[53]T. Tanaka and Y. Inuishi, J. Phys. Soc. Japan **19**, 167 (1964).
[54]J. W. Walker and C. T. Sah, Radiation Effects Journal (to be published).
[55]V. L. Bonch-Bruereich and E. G. Landsberg, Phys. Status Solidi **29**, 9 (1968), Table IV.
[56]T. H. Ning, Ph.D thesis (University of Illinois, 1970) (unpublished).
[57]W. Jung and G. S. Newell, Phys. Rev. **132**, 648 (1963).
[58]D. F. Daly, J. Appl. Phys. **42**, 864 (1971).
[59]J. R. Carter, Jr., IEEE Trans. Nucl. Sci. **13**, 24 (1966).
[60]See Ref. 43, Table IV.
[61]T. Tanaka and Y. Inuishi, J. Phys. Soc. Jap. **19**, 167 (1964).
[62]L. J. Cheng, J. C. Corelli, J. W. Corbett, and G. D. Watkins, Phys. Rev. **152**, 761 (1966).
[63]J. C. Corelli, R. C. Young, and C. S. Chen, IEEE Trans. Nucl. Sci. **17**, 128 (1970).
[64]C. A. J. Ammerlaan and G. D. Watkins, Phys. Rev. B **5**, 3988 (1972).
[65]D. K. Wilson, IEEE Trans. Nucl. Sci. **15**, 77 (1968).

PHYSICAL REVIEW B VOLUME 7, NUMBER 10 15 MAY 1973

# Schottky-Barrier Electroreflectance: Application to GaAs

D. E. Aspnes and A. A. Studna
*Bell Laboratories, Murray Hill, New Jersey 07974*
(Received 9 November 1972)

We describe a Schottky-barrier electroreflectance (ER) technique for making high-resolution optical spectroscopic measurements on semiconducting materials. When combined with recent line-shape theories of low-field ER spectra, the method provides order-of-magnitude improvement in resolution of structure and accuracy in the determination of critical-point energies and broadening parameters as compared to previous spectroscopic work on higher interband transitions. The Schottky-barrier technique is applied to GaAs, where separate critical-point contributions of $\Gamma$ and $\Delta$ symmetry in the $E_0'$ triplet are resolved for the first time, together with all members of the quadruplet at $X$. We find the values of critical-point energies $E_g$ and broadening parameters $\Gamma$ for the following transitions at 4.2 °K (all energies are in meV): $E_0$(1517.7 $\pm$ 0.5, < 0.3); $E_0 + \Delta_0$(1859 $\pm$1,6 $\pm$ 2); $E_1$(3043.9 $\pm$ 1, 28 $\pm$ 1); $E_1 + \Delta_1$(3263.6 $\pm$ 1, 38 $\pm$ 2); $E_0'$ triplet, $\Gamma$ symmetry: (4488 $\pm$ 10, < 40 $\pm$ 5), (4659 $\pm$ 10, 30 ± 5), (5014 $\pm$ 15, 47 $\pm$ 10); $E_0''$ triplet, $M_1$ transitions, $\Delta$ symmetry: (4529 $\pm$ 10, < 36 $\pm$ 5) and (4712 $\pm$ 10, 34 ± 5); $E_2$ complex, $\Sigma$: (5137 $\pm$ 10, 104 $\pm$ 10); $E_2$ complex, $X$ quadruplet: (4937 $\pm$ 10, 47 $\pm$ 10), (5014 $\pm$ 10, 47 $\pm$ 10), (5339 $\pm$ 10, 48 $\pm$ 10), (5415 $\pm$ 15, 50 $\pm$ 15). These values enable us to determine the following spin-orbit-splitting energies: $\Delta_0 = 341 \pm 2$ meV, $\Delta_1 = 220 \pm 2$ meV, $\Delta_0'$(at $\Gamma$) $= 171 \pm 15$ meV, $\Delta_0''$(at $\Delta$) $= 183 \pm 15$ meV, and $\Delta_2 = 77 \pm 10$ meV. The splitting of the lower conduction bands at $X$ due to the antisymmetric potential is $\Delta_2' = 402 \pm 10$ meV. The $E_0'$ transitions of $\Delta$ symmetry are shown to lie about 10% of the way from $\Gamma$ to $X$. By comparing the period of the large number of Franz-Keldysh oscillations observed at the $E_1 + \Delta_1$ transition with those of the $E_0 + \Delta_0$ transitions observed in the high-field measurements, we determine a value $\mu_T = (0.055 \pm 008)m_e$ for the transverse reduced mass at $E_1 + \Delta_1$. These results are compared to previous experimental measurements and to calculated energy-band structures for GaAs. The determination of critical-point symmetry in surface-barrier geometries in terms of the transformation properties of the third- and fourth-rank low-field ER line-shape tensors is also discussed. Finally, the vanishing of an ER spectrum at a hyperbolic critical point, a reduced-mass effect predicted by the general theory of the Franz-Keldysh effect, is observed for the first time.

## I. INTRODUCTION

Since the discovery of the electroreflectance (ER) effect in 1964,[1] numerous forms of modulation spectroscopy have been developed and great progress has been made in optical spectroscopy of solids.[2] As a result, much information has been obtained about the energy band structure and critical-point spectra of a wide variety of materials.[2,3] Recently, it has been shown that the sharp and richly structured ER spectra obtained at sufficiently low values of the modulating field arise from highly resonant fourth-rank-tensorial field-induced changes in the linear dielectric function.[4,5] These line shapes are closely related to the third derivative of the unperturbed dielectric function,[5-7] and thus are more directly suitable to high-resolution spectroscopy than other forms of modulation spectroscopy which yield broader first-derivative spectra.

Since low-field ER line shapes simply scale quadratically in the applied modulating field, depletion-barrier modulation is particularly well suited to high-resolution spectroscopy of semiconducting materials.[8] In addition to minimizing field-inhomogeneity effects,[9,10] the quadratic field dependence can be combined with the square-root dependence of the field on modulation potential in a fully depleted (nonequilibrium) space-charge region to yield spectra which are linear in the applied po-

tential, rather than the field, and thus are rigorously independent of modulation waveform and dc bias effects. The metal-semiconductor (MS) or Schottky-barrier ER configuration is ideal for this purpose,[8] possessing distinct advantages with respect to other surface-barrier techniques using $p$-$n$ junction, heterojunction, electrolyte, metal-oxide-semiconductor (MOS), or field-effect configurations. Schottky diodes are majority-carrier devices relatively insensitive to surface states, are particularly easy to fabricate, can be applied to a wide variety of semiconducting materials, and permit ER measurements to be made over wide ranges of temperature and wavelength.

It is the purpose of this paper to discuss the Schottky-barrier technique as a means of obtaining high-resolution ER spectra, and to apply it to GaAs. Despite intensive investigation of metal-semiconductor junctions as rectifying contacts for use in electrical devices and optical detectors,[11] the Schottky-barrier configuration has been used only occasionally in electroabsorption[12,13] and its application to ER appears to be new.[8] The primary reason for this appears to be due to the commonly accepted belief that quantitative ER spectra can only be obtained by modulation from the flat-band or zero-surface-field condition, because of the strongly nonlinear dependence of ER spectra on the modulating field. The flat-band condition cannot be obtained in a Schottky diode due to the internal barrier potential and the majority-carrier nature of the device. The proof that quantitative ER spectra can be obtained without the need for modulation from flat band, which provided the justification needed for the use of this configuration, has only recently been given.[8]

In this paper, we shall concentrate on a single material, GaAs, in order to discuss the technique and analysis of Schottky-barrier ER spectra. GaAs lacks inversion symmetry and therefore has a much more richly structured ER spectrum than group-IV materials such as Ge or Si. Moreover, the various types of optical spectra of GaAs have been well studied,[14-38] which allows us to make a direct and revealing comparison of the Schottky-barrier ER technique to other forms of optical spectroscopy. We shall show that the order-of-magnitude improvement in resolution attainable at higher interband transitions with this technique enables us to obtain a wide variety of new information. For example, we have identified and measured critical-point energies and broadening parameters for a number of transitions never before resolved, and have also measured the transverse mass of the $E_1+\Delta_1$ transition.

The outline of the paper is as follows: In Secs. II A and II B, experimental details of sample preparation, measurement techniques, and data processing are discussed. Section II C deals with electrical properties. In Sec. II D, symmetry analysis is discussed in terms of the transformation properties of third- and fourth-rank tensors in diamond and zinc-blende crystals. The data are presented and analyzed in Sec. III, with the main spectroscopic results being summarized in Table II. Finally, in Sec. IV we compare our results to other measurements and calculations of the energy-band structure of GaAs. Relevant equations are summarized in the Appendix.

## II. EXPERIMENTAL

### A. Sample Construction

The Schottky-barrier ER technique depends on the formation of a Schottky barrier or MS diode when a thin, semitransparent metal film is deposited on the front or reflecting surface of the semiconductor. Schottky barriers can be formed on a wide variety of semiconducting materials, as tabulated in Sze.[39] Since the metal film must be semitransparent, the choice of metal is dictated in part by the requirement that it be relatively inert (not readily oxidized or corroded) under ambient conditions. We have found Au and Ni to be particularly well suited for ER applications. Although Ni tends to oxidize in air, its relatively uniform transmittivity over a wide spectral region gives it an advantage over Au from a spectroscopic point of view, since Au has substantial structure in its optical spectrum around 2.5 eV.[40]

Samples used in these experiments consisted of $n$-type single crystals of GaAs of carrier concentration of the order of the optimum value of $10^{16}$ $cm^{-3}$.[8] The back surface of the samples was sand-blasted or mechanically abraded in order to introduce recombination centers and eliminate the possibility of back-surface specular reflection below the fundamental absorption edge, which can result in spurious signals in modulated reflectivity spectra due to electroabsorption effects.[24] Electrical contact was made to this back surface by rhodium plating.[41] This contact was durable, strain-free, Ohmic, and showed negligible resistance ($<1\,\Omega$) under all measurement conditions reported herein, indicating contact was being made directly to the semiconductor with no intervening high-resistivity oxide layer[42] being present. A highly specular, relatively damage-free front surface was obtained by Syton[43] polishing. The sample edges were masked and the metal film was deposited over an area of roughly $5\times9$ mm in the pressure range of $3\times10^{-6}$ Torr as soon as possible following polishing in order to minimize the thickness of the natural-surface-oxide layer.[44] The metal thickness was monitored by measuring the resistance between two contacts at the ends of a quartz slide adjacent to the sample, and evaporation was terminated at a

measured resistance of 1000 Ω/□. The single-pass transmittance of Ni films prepared in this manner was typically of the order of 75–80%, corresponding to a calculated thickness of about 3.5 nm. The completed samples were therefore essentially laminar structures consisting of a back contact, the semiconductor crystal, a very thin natural-oxide layer on the semiconductor, a semitransparent metal film, and a thin metal-oxide layer adjacent to the ambient. The existence of the natural-oxide layer between the semiconductor crystal and metal film could be inferred from pumpdown time delays in the fabrication process, known growth rates of semiconductor oxides under atmospheric conditions,[44] and the observation of Ohmic behavior (~1000 Ω cm$^2$) of the diode under large forward bias.[42,45] In contrast to the MOS ER technique,[46] this oxide was sufficiently electrically transparent so as not to influence the basic metal-semiconductor nature of the junction. The existence of a thin nickel-oxide film on the ambient side of the Ni film was suggested by the observation that the resistance of the equivalent Ni film deposited on the quartz slide always increased when the slide was exposed to air. While the nickel oxide had no detectable deleterious short-term effect on the electrical or optical response of the MS diodes, oxidation obviously progressed slowly since diodes prepared with Ni films generally became unusable after several weeks.

### B. Measurement Techniques

Electroreflectance spectra were measured with standard optical and phase-sensitive electronic detection equipment using techniques well documented in the literature.[47] The optical system for measurements above 2 eV consisted of an Illumination Industries model XBO-75 xenon short-arc lamp, a Jarrell-Ash 1-m monochromator, an Air Products LT-3 cryotip refrigerator for sample mounting and temperature control, an RCA 7200 photomultiplier, and a Kepco model BHK-2000-0.1M power supply electronically regulated with a 0.3-sec time constant to maintain 100-μA average current flow at the photomultiplier anode. For lower-energy measurements, the light source and detector were replaced with a Sylvania FCS quartz-halogen lamp and an RCA C31025C GaAs-cathode photomultiplier regulated to 5-μA average anode current. Polarization measurements were made with a calcite polarizer or Polaroid HNB'P unsupported uv polarizing film. The sample was mounted on the cold finger of the cryotip with silver paint[48] applied uniformly over the back contact. This technique provided a good electrical ground and a good thermal contact while inducing virtually no strain in the sample. This was verified (somewhat to our surprise) by observing the extremely sharp and strain-sensitive $n=1$ exciton line in GaAs at 1513.5±0.5 meV, in excellent agreement with transverse exciton polariton peak at 1514.8 meV reported by Sell *et al.*[30] in measurements on high-purity rigorously strain-free, epitaxially grown samples (the 1-meV discrepancy is due primarily to impurity effects[36] in our less pure bulk samples). The dc bias and 150-Hz square-wave ac modulation voltages were added potentiostatically and applied to the semitransparent metal layer by means of a thin wire attached to the metal film with a dot of silver paint.

The detection and data-processing system included a Princeton Applied Research model HR-8 phase-sensitive detector, a Hewlett-Packard model 5480 signal averager, a Hewlett-Packard model 2114 computer, and a Sykes model 100 cassette recorder. The system operated as follows: The operator provided the low- and the high-energy limits of the desired spectrum as input data. The computer divided the specified energy range into 249 equal-energy increments, corresponding to the energy separation between pairs of the 250 data points spanning the spectrum. The computer then drove the monochromator by means of a stepping motor to the wavelength corresponding to the high-energy end point of the spectrum (the wavelength-energy conversion factor 1.239 513 eV μ was used[36]). When this wavelength had been reached, the monochromator halted and the signal averager began sampling the output of the phase-sensitive detector with the wavelength held constant. The sampling was typically done at a 1250 point-per-second rate, until the number of 250-point sampling sweeps preset by the operator (usually between $2^0$ and $2^6$) had been accumulated. The time constant of the phase-sensitive detector was usually set at 100 msec, so that signal-to-noise enhancement was performed by the signal averager rather than by the phase-sensitive dector. When the signal averaging was completed at the given wavelength, the computer stored in memory the data point thus obtained, cleared the signal averager, and drove the monochromator to the wavelength corresponding to the energy of the next data point in the spectrum. The process was repeated until the complete spectrum had been obtained. These spectra were stored on magnetic tape for later data processing on the computer, if desired. We have found this technique to be significantly better than the usual method, where the monochromator wavelength increases at a constant rate while the output of the phase-sensitive detector is plotted by an $x$-$y$ or strip-chart recorder, for a number of reasons. First, when the monochromator wavelength is increased at a constant rate, there is always a compromise between the rate of change of the average detector output due to spectral features and the amount of signal

averaging obtainable from the time constant of the phase-sensitive detector. Too fast a scanning rate can result in a severe distortion of spectra due to the "memory" effect of the $RC$ averaging circuits of the phase-sensitive detector, while too slow a scanning rate wastes time and results in an excessive amount of noise on the spectra for a given measurement period. By using the signal averager rather than the phase-sensitive detector to perform the signal-averaging function in the incremental-wavelength-advance technique used here, spectral distortion is completely eliminated while signal enhancement is utilized fully. Second, spectra linear in energy are obtained directly. Third, it is possible to average digitally a series of spectra taken under the same conditions, and thus eliminate the judgment factor in smoothing experimental curves.[49]

### C. Determination of Modulation Conditions

For quantitative interpretation of experimental data, it is necessary to know the conditions under which the ER spectra are obtained. Thus it is necessary to determine the surface field, the spatial homogeneity of sample doping, whether a fully depleted barrier is actually formed, and whether nominally low-field spectra are really low-field spectra, that is, scale quadratically with the applied field. We briefly discuss these points in this section.

The existence of a fully depleted barrier and an indication of the sample impurity concentration and surface field can be determined from the equations describing the electrical properties of an ideal fully depleted (nonequilibrium) space-charge region formed in conjunction with a rectifying contact on an $n$-type semiconductor.[50] These equations are

$$J = J_0 (e^{eV_{ext}/kT} - 1) \ , \tag{2.1a}$$

$$\mathcal{E}_s^2 = (2eN_D/\epsilon_0)(-V_{int} - V_{ext} - kT/e) \ , \tag{2.1b}$$

$$C^{-2} = (2/e\,\epsilon_0 N_D)(-V_{int} - V_{ext} - kT/e) \ , \tag{2.1c}$$

where $J$ is the current density, $V_{ext}$ is the externally applied potential, $J_0$ is a coefficient which is a function of $V_{ext}$ and $T$ but which varies slowly with respect to the exponential term in Eq. (2.1a), $\mathcal{E}_s$ is the surface field, $N_D$ is the electrically active carrier concentration (which is frequency dependent in compensated crystals or crystals with deep impurity centers[51]), $\epsilon_0$ is the static dielectric constant, $V_{int}$ is the internal barrier potential, and $C$ is the space-charge capacitance per unit area. In Eqs. (2.1b) and (2.1c), $V_{ext} \ll -V_{int} - kT/e$. The coefficient $J_0$ in Eq. (2.1a) is determined primarily by majority-carrier flow over the barrier with a small contribution from minority carriers generated either by optical or thermal excitation in the space-charge region or by diffusion-limited flow from the bulk. Thus, as long as any insulating film between the metal and semiconductor is electrically thin [(back resistance)/(forward Ohmic resistance) = figure of merit $\gg 1$], the Schottky diode and the resultant ER spectrum are both exceptionally stable with respect to changes in temperature, illumination intensity, etc. Our samples satisfied this criterion; the figure of merit was at least 1000, showing good rectifying properties. As mentioned before, the observation in our samples of Ohmic behavior with resistance of $\sim 1000\ \Omega\,\mathrm{cm}^2$ for strong forward bias, together with the observation of negligible back contact resistance, provided proof[42,45] of the existence of a thin oxide layer of moderate resistivity ($10^3\ \Omega\,\mathrm{cm}^2 = 10\ \text{Å} \times 10^{10}\ \Omega$ cm), which could be ignored for measurements in the reverse-bias direction.

The existence of a depletion region can be shown in the usual manner by measuring the capacitance as a function of reverse bias. When plotted as $C^{-2}$ vs $-V_{ext}$, Eq. (2.1c) shows that a straight-line results, whose slope in principle gives the impurity concentration $N_D$. These plots were obtained for our samples by means of a high-frequency square-wave technique,[52] operating at 500 kHz. At both room temperature and 4.2°K, good straight-line dependencies of $C^{-2}$ vs $-V_{ext}$ were obtained, with barrier heights $\sim 0.9$ V (zero-bias surface field $\sim 50\ \mathrm{kV\,cm^{-1}}$). However, it was found that the carrier concentration $N_D$ calculated from these slopes did not yield values of the surface field, through Eq. (2.1b), consistent with the results obtained from two independent ER phenomena to be discussed in Sec. III: the period of the interference oscillations between the space-charge region and the bulk at the wavelength of the direct exciton at the $E_0$ edge, and the period of the subsidiary Franz–Keldysh oscillations at the $E_0 + \Delta_0$ transition. The field determined by capacitance measurements was usually of the order of 40% lower than the corresponding ER values. This discrepancy is easily explained by the frequency dependence of $N_D$,[51] since fewer deep-lying donor states should contribute to the 500-kHz capacitance measurement than to the 150-Hz ER measurement in these partially compensated materials. Consequently, for high-field results we quote field values appropriate to the ER frequency. We note that it is not usually possible to determine $N_D$ by capacitance measurements below 10 kHz, due to in-phase conductance currents, and thus the ER effect offers a means of determining this parameter in normally inacessible frequency ranges.

For low-field ER measurements, characterized by a linear dependence of the modulated reflectivity on the modulating potential,[8] accurate surface-field values are not important for energy gap and lifetime broadening measurements.[53,54] The low-field limit of the modulation potential was determined

for each transition either by a visual observation of the linear range of the real-time response, $\Delta R(t)/R$, measured by the signal averager for triangular-wave modulation, or else by applying a small fixed modulation voltage and varying the dc bias until signal degradation occurred. Samples were also checked for uniformity of doping and surface fields in the low-field range by scanning the focused output beam from the monochromator over the active region of the MS diode. The samples which we used exhibited no observable spatial dependence of the response, indicating a uniform doping and also no observable transverse voltage drop in the semitransparent metal films.

### D. Symmetry Considerations: Optimum Sample Orientation

Schottky-barrier ER spectra were obtained only for the (110) surface of GaAs. It is easy to show by very general symmetry arguments that this surface yields all the information obtainable about quadratic low-field ER spectra in a surface-barrier measurement on crystals of diamond or zinc-blende symmetry. At sufficiently low fields, ER spectra can be represented in general as third-rank-tensorial (linear-ER[25,55]) and fourth-rank-tensorial (quadratic-ER[4-6]) nonlinear optical susceptibilities of the form

$$\Delta R/R = \mathrm{Re}\{\tilde{C}[n_i n_j \mathcal{E}_k \chi_{ijk}(\hbar\omega) + n_i n_j \mathcal{E}_k \mathcal{E}_l \chi_{ijkl}(\hbar\omega)]\} \quad , \tag{2.2}$$

where $\Delta R/R$ is the measured modulation spectrum, $\tilde{C}$ is a slowly varying complex function of $\hbar\omega$, $n_i$ is the $i$th component of the unit polarization vector $\hat{n}$ of the incident radiation, $\mathcal{E}_k$ is the $k$th component of the externally applied electric field $\vec{\mathcal{E}}$, and $\chi_{ijk}(\hbar\omega)$ and $\chi_{ijkl}(\hbar\omega)$ are components of the third-rank, second-order and fourth-rank, third-order nonlinear optical susceptibility tensors $\chi^{(2)}(\omega; 0, \omega)$ and $\chi^{(3)}(\omega; 0, 0, \omega)$, respectively. Explicit expressions for $C$ and $\chi_{ijkl}(\hbar\omega)$ are given in Eqs. (A2c) and (A3) of the Appendix. The tensor indices $i, j$, $k$, and $l$ in Eq. (2.2) are summed over the three Cartesian axes $x$, $y$, and $z$, measured with respect to the crystal. In crystals of zinc-blende symmetry there is only one nonvanishing third-rank and three nonvanishing fourth-rank components of the form $\chi_{xyz} = \chi_{123}$, and $\chi_{xxxx} = \chi_{11}$, $\chi_{xxyy} = \chi_{12}$, and $\chi_{xyxy} = \chi_{44}$, respectively.[56] Crystals of diamond symmetry differ only in that $\chi_{123} \equiv 0$. Thus the most general low-field ER response in a crystal of diamond or zinc-blende symmetry can be written

$$\begin{aligned}\Delta R/R = \mathrm{Re}(\tilde{C}\{&2\chi_{123}(\hbar\omega)(n_x n_y \mathcal{E}_z + n_y n_z \mathcal{E}_x + n_z n_x \mathcal{E}_y) \\ &+ \chi_{11}(n_x^2\mathcal{E}_x^2 + n_y^2\mathcal{E}_y^2 + n_z^2\mathcal{E}_z^2) \\ &+ \chi_{12}[n_x^2(\mathcal{E}_y^2+\mathcal{E}_z^2) + n_y^2(\mathcal{E}_z^2+\mathcal{E}_x^2) + n_z^2(\mathcal{E}_x^2+\mathcal{E}_y^2)] \\ &+ 2\chi_{44}(n_x n_y \mathcal{E}_x \mathcal{E}_y + n_y n_z \mathcal{E}_y \mathcal{E}_z + n_z n_x \mathcal{E}_z \mathcal{E}_x)\}) \quad . \end{aligned} \tag{2.3}$$

Note that the quadratic terms have formally the same structure as encountered in the theory of piezoreflectance,[57,58] with the dyadic vector product $\mathcal{E}_i \mathcal{E}_j$ taking the place of the second-rank strain-tensor component $e_{ij}$. Thus, an analysis of the symmetry properties of quadratic low-field ER spectra, completely equivalent to Kane's analysis[57] of piezoreflectance, can be given. The above treatment is also similar to treatments of the symmetry problem in ER on the basis of the general Franz–Keldysh equations.[24,59,60]

To show that a {110} surface is the optimum surface for measuring the quadratic ER effect in any surface-barrier configuration, we show first that there exists *no* condition which enables all three fourth-rank tensor coefficients $\chi_{11}$, $\chi_{12}$, and $\chi_{44}$ to be separately determined in a surface-barrier ER experiment. We square the defining condition of surface-barrier ER to find

$$\begin{aligned}(\hat{n}\cdot\vec{\mathcal{E}})^2 = 0 \\ = (n_x^2\mathcal{E}_x^2 + n_y^2\mathcal{E}_y^2 + n_z^2\mathcal{E}_z^2) \\ + 2(n_x n_y \mathcal{E}_x \mathcal{E}_y + n_y n_z \mathcal{E}_y \mathcal{E}_z + n_z n_x \mathcal{E}_z \mathcal{E}_x) \quad . \end{aligned} \tag{2.4}$$

Equation (2.4) shows that the tensorial functions multiplying the coefficients $\chi_{11}$ and $\chi_{44}$ in Eq. (2.3) are always equal and opposite in sign in a surface-barrier geometry. Therefore, $\chi_{11}$ and $\chi_{44}$ can be determined only in the linear combination $\chi_{11} - \chi_{44}$ in a surface-barrier configuration. The optimum surface is next obtained by evaluating Eq. (2.3) for the three simplest crystallographic orientations. The results are shown in Table I. For {100} surfaces, the isotropic component of $\Delta R/R$ comes entirely from the fourth-rank coefficient $\chi_{12}$, while the polarization dependence arises entirely from the linear term $\chi_{123}$. Thus, surface-barrier measurements on {100} surfaces provide an alternate to harmonically analyzed transverse ER (TER) measurements[25] in determining the line shape of the linear component.[25,55] For {110} surfaces the *linear* contribution is identically zero, and the polarization dependence arises from the quadratic coefficients in the irreducible combination $\chi_{11} - \chi_{44}$ and $\chi_{12}$. $\Delta R/R$ for {111} surfaces contains both linear and quadratic contributions and shows no polarization dependence. Since no general theory for the spectral dependence of the linear term $\chi^{(2)}_{123}(\hbar\omega)$ is yet available, we have restricted our measurements reported here to the (110) surface.

## III. RESULTS

### A. $E_0$ and $E_0 + \Delta_0$ Transitions

Schottky-barrier ER spectra obtained in the region of the $E_0$ and $E_0 + \Delta_0$ transitions are shown in Fig. 1. These are typical 4.2°K spectra, here taken with the barrier under forward bias with the

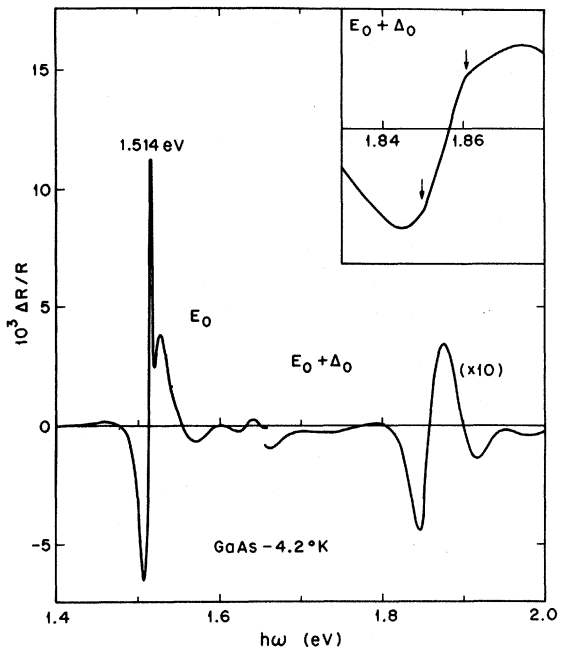


FIG. 1. Schottky-barrier ER spectrum of the $E_0$ and $E_0+\Delta_0$ transitions of GaAs, taken under conditions described in the text. Inset: expanded view of the exciton structure associated with the $E_0+\Delta_0$ transition.

150-Hz square-wave voltage levels at + 1.4 and +5.5 V. The more positive voltage results in a substantial current flow and appears as *IR* voltage drops in the circuit, rather than across the space-charge region. The value +1.4 V corresponds roughly to the lowest practical characterized surface field which could be obtained on this sample. The appearance of subsidiary oscillations at energies above the dominant structure for both transitions indicates that even for these low fields, the modulation was effectively high-field modulation. This is simply due to the small broadening parameters of these transitions.

The $E_0$ spectrum is dominated by the transverse exciton-polariton structure at 1513.5 ± 0.5 meV in this sample. Since only one such structure is observed at an energy which agrees well with the value 1514.8 meV measured in a high-purity epitaxial film by Sell *et al.*,[30] this indicates that the sample was essentially strain free, as mentioned in Sec. II. Using the calculated value of the exciton binding energy, 4.2 meV, yields the critical-point energy $E_g = 1517.7$ meV. The observed width of the peak, $2\Gamma = 0.6$ meV [full width at half-maximum (FWHM)], is determined by the resolution of the monochromator and is not characteristic of the actual broadening of the transition, which is much less.[37] The results are given in Table II, along with those of other relevant experiments.

The entire exciton structure seen in ER at the $E_0$ edge is strongly voltage dependent. Measurements of the differential reflectance change as a function of bias voltage for any *fixed* wavelength in the vicinity (± 25 meV) of the peak energy at 1513.5 meV yield a series of oscillations which decrease in amplitude as the depletion bias is increased. These oscillations are shown in Fig. 2. This type of interference phenomenon is well known in ER and arises from an optical mismatch between the space-charge region and the bulk, which may be caused by a variety of factors such as free-carrier absorption[61] or, as is the case here, by exciton dissociation in the field of the space-charge region, as has been seen previously in CdS by Tyagai *et al.*[62] The decrease in amplitude of the interference oscillations with increasing reverse bias, evident in Fig. 2, is simply due to the increase in total optical absorption of the reflected beam as the space charge region extends deeper into the bulk.

It is interesting to note that the residual optical absorption in the space-charge region is strongly influenced by the barrier field. This follows directly from the experimental observation that the

TABLE I. Explicit form of the linear term and sum of quadratic terms in the bracketed part of Eq. (2.3) for the three simplest crystallographic orientations in a surface-barrier geometry for crystals of zinc-blende symmetry. The unit field vector $\hat{g}$ is normal to the surface, and the unit polarization vector $\hat{n}$ lies in the plane of the surface. $\theta$ is the polarization angle of the incident radiation measured with respect to the crystallographic reference direction indicated. For crystals of diamond symmetry, $\chi_{123} \equiv 0$.

| Surface | (100) | (110) | (111) |
|---|---|---|---|
| $\hat{g}$ | $(1,0,0)$ | $(1,1,0)/\sqrt{2}$ | $(1,1,1)/\sqrt{3}$ |
| $\hat{n}$ | $(0,\sin\theta,\cos\theta)$ | $(\sin\theta/\sqrt{2},-\sin\theta/\sqrt{2},\cos\theta)$ | $(\cos\theta/\sqrt{2}+\sin\theta/\sqrt{6},-\cos\theta/\sqrt{2}+\sin\theta/\sqrt{6},-2\sin\theta/\sqrt{6})$ |
| Reference direction for $\theta$ | $\hat{z}$ | $\hat{z}$ | $(\hat{x}-\hat{y})/\sqrt{2}$ |
| Linear term | $\chi_{123}\sin 2\theta$ | 0 | $-2\chi_{123}/\sqrt{3}$ |
| Sum of quadratic terms | $\chi_{12}$ | $(\chi_{11}-\chi_{44})\sin^2\theta+\frac{1}{2}\chi_{12}(1+\cos^2\theta)$ | $[(\chi_{11}-\chi_{44})+2\chi_{12}]/\sqrt{3}$ |

TABLE II. Experimentally determined values of critical point parameters of GaAs at low temperatures as obtained from Schottky-barrier ER, wavelength-derivative reflectance (WDR), wavelength-modulated reflectance (WMR), transverse electroreflectance (TER), and thermoreflectance (TR) measurements.

| Transition | Quantity | Schottky-barrier ER (4.2 °K) (meV) | Sell *et al.* WDR (2 °K) (meV) | Zucca and Shen WMR (5 °K) (meV) | Kyser and Rehn TER (85 °K) (meV) | Welkowsky and Braunstein WMR (80 °K) (meV) | Matatagui *et al.* TR (80 °K) (meV) |
|---|---|---|---|---|---|---|---|
| $E_0$ | $E_{ex}$ | 1513.5 ± 0.5 | 1515.0[a,b] | | | | |
| $\Gamma_8^v \rightarrow \Gamma_6^c$ | $\Gamma$ | < 0.3 | 0.1[c] | | | | |
| | $E_g$ | 1517.7 ± 0.5[d] | 1519.2 ± 0.2[c] | | | | 1460[g,k] |
| $E_0 + \Delta_0$ | $E_{ex}$ | 1855 ± 1 | 1855 ± 2[e] | | | | |
| | $\Gamma$ | 6 ± 2 | 10[e] | | | | |
| $\Gamma_7^v \rightarrow \Gamma_6^c$ | $E_g$ | 1859 ± 1[d] | 1859 ± 2[d] | | | | 1800[g,k] |
| | $\Delta_0$ | 341 ± 2 | 340 ± 2 | | | | 340 |
| $E_1$ | $\Gamma$ | 28 ± 1 | | | 31 ± 2[h] | | |
| $\Lambda_4^v \rightarrow \Lambda_6^c$ | $E_g$ | 3043.9 ± 1 | | 3017 ± 4[f,g] | 3042 ± 3[h] | 2981[g,j] | 2950[g,k] |
| $E_1 + \Delta_1$ | $\Gamma$ | 38 ± 2 | | | 38 ± 2[h] | | |
| $\Lambda_6^v \rightarrow \Lambda_6^c$ | $E_g$ | 3263.6 ± 1 | | 3245 ± 4[f,g] | 3266 ± 3[h] | 3211[g,j] | 3190[g,k] |
| | $\Delta_1$ | 220 ± 2 | | 228 ± 8 | 224 ± 6 | 230 | 240 |
| $E_0'(\Gamma)$ | $\Gamma$ | < 40 ± 5[g] | | | | | |
| $\Gamma_8^v \rightarrow \Gamma_7^c$ | $E_g$ | 4488 ± 10 | | | | | |
| $E_0'(\Delta)$ | $\Gamma$ | < 36 ± 5[g] | | | | | |
| $\Delta_5^v \rightarrow \Delta_6^c$ | $E_g$ | 4529 ± 10 | | 4440 ± 8[f,g] | 4510 ± 30[i] | 4520[g,j] | 4500[g,k] |
| $E_0' + \Delta_0'(\Gamma)$ | $\Gamma$ | 30 ± 5 | | | | | |
| $\Gamma_8^v + \Gamma_8^c$ | $E_g$ | 4659 ± 10 | | | | | |
| | $\Delta_0'$ | 171 ± 15 | | | | | |
| $E_0' + \Delta_0'(\Delta)$ | $\Gamma$ | 34 ± 5 | | | | | |
| $\Delta_5^v \rightarrow \Delta_5^c$ | $E_g$ | 4712 ± 10 | | 4600 ± 8[f,g] | | 4720[g,j] | 4800[g,k] |
| | $\Delta_0''$ | 183 ± 15 | | 160 ± 16 | | | |
| $E_0' + \Delta_0' + \Delta_0$ | $\Gamma$ | 47 ± 10 | | | | | |
| $\Gamma_7^v \rightarrow \Gamma_8^c$ | $E_g$ | 5014 ± 15 | | | | | |
| | $\Delta_0$ | 355 ± 20 | | | | | |
| $E_2$ | $\Gamma$ | 104 ± 10 | | | | | |
| $\Sigma$ | $E_g$ | 5137 ± 10 | | 5110 ± 10[f,g] | | | 5050[g,k] |
| $E_2$ | $\Gamma$ | 4937 ± 10 | | | | | |
| $X_7^v \rightarrow X_6^c$ | $E_g$ | 47 ± 10 | | | | | |
| | $\Gamma$ | 47 ± 10 | | | | | |
| $E_2$ | $E_g$ | 5014 ± 10 | | | | | |
| $X_6^v \rightarrow X_6^c$ | $\Delta_2$ | 77 ± 10 | | | | | |
| | $\Gamma$ | 48 ± 10 | | | | | |
| $E_2$ | $E_g$ | 5339 ± 10 | | 5640(?) ± 30[f,g] | | | |
| $X_7^v \rightarrow X_7^c$ | $\Delta_2'$ | 402 ± 10 | | | | | |

TABLE II. (*Continued*)

| Transition | Quantity | Schottky-barrier ER (4.2 °K) (meV) | Sell *et al.* WDR (2 °K) (meV) | Zucca and Shen WMR (5 °K) (meV) | Kyser and Rehn TER (85 °K) (meV) | Welkowsky and Braunstein WMR (80 °K) (meV) | Matatagui *et al.* TR (80 °K) (meV) |
|---|---|---|---|---|---|---|---|
| $E_2$ | $\Gamma$ | 50 ± 15 | | | | | |
| | $E_g$ | 5415 ± 15 | | | | | |
| $X_6^v \rightarrow X_7^c$ | $\Delta_2$ | 76 ± 15 | | | | | |
| | $\Delta_2'$ | 400 ± 15 | | | | | |

[a]Reference 30.
[b]Reference 36.
[c]Reference 37.
[d]Calculated value; see text.
[e]Reference 28; see also Ref. 68.
[f]Reference 26.
[g]Energy of reflectivity peak.
[h]Calculated from data in Ref. 25; see text.
[i]Calculated from data in Ref. 33.
[j]Reference 32.
[k]Reference 22.

envelope of the interference effect is larger (of the order of 25%) for light polarized in the $[1\bar{1}0]$ direction than in the [001] direction under conditions of equal illumination intensity, together with the calculation by Keldysh *et al.*[63] of polarization anisotropies in electroabsorption which arise from the degeneracy-induced warping of the upper valence bands in diamond and zinc-blende semiconductors. We find from Eq. (48) of Ref. 63 that the polarization-dependent prefactor for the electric-field-induced absorption coefficient below the fundamental absorption edge can be written

$$\alpha \sim \tfrac{1}{3}[(\gamma_2^2+3\gamma_3^2)^{1/2}-\gamma_2]+\tfrac{1}{2}(\gamma_2-\gamma_3)\sin^2\theta$$
$$= 1.25 - 0.44\sin^2\theta \ , \qquad (3.1)$$

using the Luttinger Hamiltonian parameters $\gamma_2 = 2.41$ and $\gamma_3 = 3.28$ as calculated for GaAs by Lawaetz.[64] Here, $\theta$ is the angle between the polarization vector and the [001] reference axis, as used in Table I. It is evident from Eq. (3.1) that the total absorption coefficient of the space-charge region should be greater for polarization along [001] ($\theta = 0°$) than along $[1\bar{1}0]$ ($\theta = 90°$) if an electroabsorption component is present. This is in agreement with our results, and has also been verified by Berozashvili *et al.* in a direct electroabsorption measurement.[31] Since the space-charge field is spatially dependent and since excitonic effects influence the magnitude of the electroabsorption prefactor,[65-67] it is not feasible to analyze this effect quantitatively. We note, however, that the magnitude of the anisotropy given in Eq. (3.1) is easily

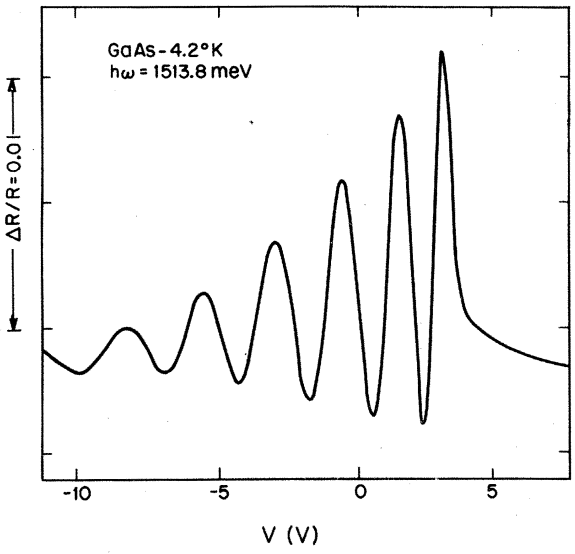


FIG. 2. Interference oscillations in the real-time relative reflectivity change $\Delta R(t)/R$ due to exciton quenching in the space-charge region. Experimental conditions: wavelength constant, corresponding to $\hbar\omega = 1513.5$ meV; 150-Hz triangular modulation from −11.3 to +7.5 V.

capable of producing the experimentally observed anistropy ratio in view of the approximate depth of the space-charge region.

The $E_0+\Delta_0$ transition exhibits two anomalous breaks in the otherwise smoothly varying ER spectrum, at 1850 and 1861 meV, as shown in the inset in Fig. 1. We attribute these features to the $n=1$ exciton at this threshold, which influences the ER spectrum by means of the same interference phenomenon causing the sharp exciton structure at the $E_0$ threshold. The structure here is significantly weaker due to the increased lifetime broadening and absorption coefficient appropriate to the higher-energy transition. The exciton contribution in the inset is evidently of the form of the dispersion curve rather than the Lorentzian line shape of the corresponding structure at the $E_0+\Delta_0$ transition. This line-shape difference is simply due to the fact that the dissociation fields for the two excitons differ by nearly an order of magnitude, whence the effective boundary between space-charge region and bulk for the $E_0+\Delta_0$ exciton interference effect is much closer to the surface than for the $E_0$ exciton. From the characteristics of the dispersion curve, $\mathrm{Re}[(E-E_{ex}+i\Gamma)^{-1}]$, we calculate the $n=1$ exciton energy $E_{ex}$ and broadening parameter $\Gamma$ to be $1855\pm1$ and $6\pm2$ meV, respectively, for this transition at 4.2°K. This is in agreement with the wavelength-derivative reflectance (WDR) measurements by Sell and Stokowski.[28,68] The spin-orbit splitting $\Delta_0$ can be calculated accurately from the above data and the value of the $n=1$ binding energy at the $E_0+\Delta_0$ transition, which can be obtained from the effective-mass approximation. Using the effective-mass values $m_c^*=0.067m_e$ and $m_{so}^*=0.15m_e$ given by Lawaetz,[64] together with the static dielectric constant of 13.5 for GaAs, we find 3.4 meV for the binding energy. Thus $\Delta_0=341\pm2$ meV at 4.2°K. These data are also given in Table II.

The threshold energy values obtained by Sell *et al.*[30,36] for the $E_0$ transition are more representative of pure GaAs simply because the epitaxial samples used in the WDR measurement were substantially purer ($N_D\sim10^{15}$ cm$^{-3}$) than the bulk samples used in the Schottky-barrier ER measurements ($N_D\sim10^{16}$ cm$^{-3}$). The 1-meV shift of the exciton line shape to lower energies in our measurements is a result of this higher impurity content.[36] The WDR data are compatible with the ER data at $E_0+\Delta_0$, as seen in Table II.

### B. $E_1$ and $E_1+\Delta_1$ Transitions

At large values of lifetime broadening, ER is clearly the optimum modulation technique. Schottky-barrier ER spectra obtained in the region of the $E_1$ and $E_1+\Delta_1$ transitions are shown in Fig. 3. The top set of curves shows three representative low-field curves, two corresponding to the

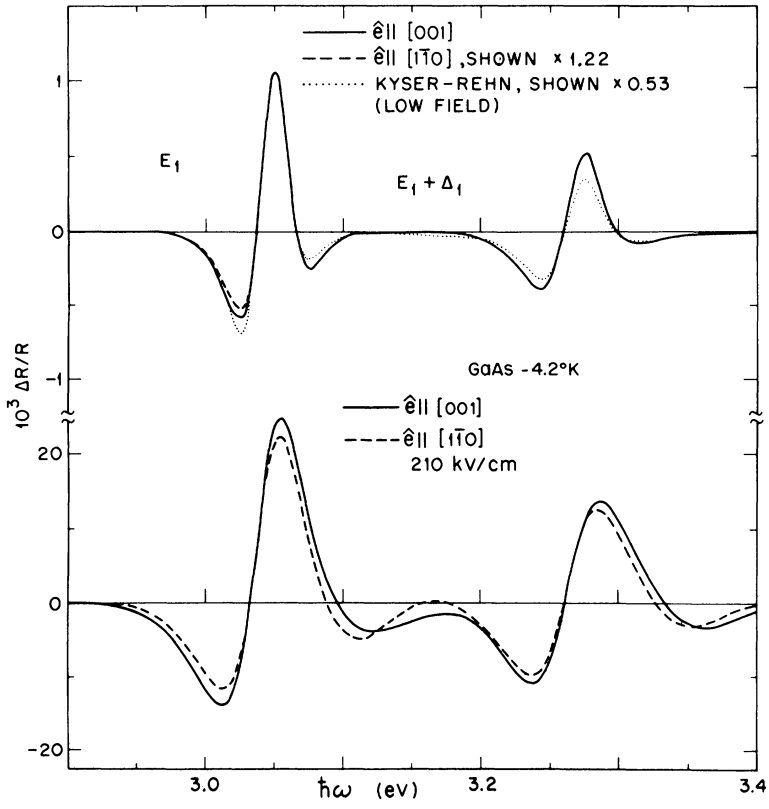


FIG. 3. Schottky-barrier ER spectra for GaAs at 4.2 °K, taken at low and relatively high values of the surface field in the energy range of the $E_1$ and $E_1+\Delta_1$ transitions, for the two principal polarizations on the (110) surface. The low-field spectrum obtained with $\hat{n}\parallel[1\bar{1}0]$ has been scaled by 1.22 as shown in order to bring the positive extrema into coincidence. The TER data of Ref. 25, taken at 85 °K, has been fitted similarly with a scaling factor of 0.53, and has been superimposed on the surface-barrier spectra for comparison.

same low-field conditions, $\mathcal{E}_s \sim 20$–$30$ kV cm$^{-1}$, at 4.2 °K in the Schottky-barrier configuration but for the two principal orthogonal polarizations, $\hat{n} \parallel [1\bar{1}0]$ and $\hat{n} \parallel [001]$, and the third, with $\mathcal{E}_s = 23$ kV cm$^{-1}$, taken by Kyser and Rehn in the TER configuration. The TER and $\hat{n} \parallel [1\bar{1}0]$ curves have been scaled by factors of 0.53 and 1.22, respectively, to bring all positive $E_1$ extrema into coincidence. The bottom pair of curves show the Schottky-barrier ER spectra for the two principal orthogonal polarizations taken at a relatively high field, 210 kV cm$^{-1}$. The field-induced broadening of the high-field spectra with respect to the low-field results is evident by inspection.

We consider first the determination of the band structure parameters $E_g$, $\Gamma$, and $\Delta_1$ for the transitions $E_1$ and $E_1+\Delta_1$. This procedure differs from that used for the $E_0$ and $E_0+\Delta_0$ spectra, because no discrete exciton structure is present. The broadening energy $\Gamma$ and the critical-point energy $E_g$ can be determined most accurately from the low-field curves of Fig. 3. It is known from band-structure calculations[27,69–72] that $\mu_T \ll |\mu_L|$, i.e., that for most calculations these transitions can be represented adequately as two-dimensional critical points. However, a recent analysis[6] on low-temperature ER measurements in Ge has suggested that each of these critical points obtain contributions from three-dimensional critical points of types $M_0$, located at the $L$ point, and $M_1$, located somewhere within the zone along the $\Lambda$ symmetry axis. Accordingly, we have calculated $E_g$ and $\Gamma$ for both transitions by least-squares fitting both three- and two-dimensional-model low-field line shapes, given by Eqs. (A8) and (A9) of the Appendix, over a 60-meV interval centered on the dominant structure. We find $E_g$ is the *same* (±0.5 meV) for both model densities of states for both transitions, as expected from an analysis of the properties of the general class of complex resonance line shapes.[53,54] However, the best-fit broadening parameters differ by about 20%, being larger for the intrinsically sharper two-dimensional (2D) structure. Since the 2D line shape contains inherently more structure, we have used Eq. (A9) to determine the parameters of these transitions listed in Table II. Also given in Table II are the values obtained by applying the same analysis to the TER data taken at 85 °K by Kyser and Rehn,[25] shown superimposed on the low-field data of Fig. 3, and values quoted from other representative experiments in the literature.

We consider next the implications of the very good agreement between the 85 °K TER spectrum of Kyser and Rehn,[25] and our 4.2 °K Schottky-barrier ER spectra, as shown in Table II and Fig. 3. Although the former data were taken at a higher temperature, it is not so high that either $E_g$ or $\Gamma$ has changed appreciably; the intrinsically sharper $E_1$ spectrum shows a slightly larger broadening at the higher temperature, as could be expected. All spectra were taken at essentially the same values of surface field; optical attenuation accounts for nearly all of the scaling factor used in Fig. 3. The good agreement in broadening parameters shows directly that surface normal fields in this TER measurement were small compared to the value of 23 kV cm$^{-1}$ given in Ref. 25 for this spectrum. Any surface normal field exceeding the low-field value would cause field-induced broadening of the type obvious in the lower pair of spectra in Fig. 3. The upper limit on "low" fields can be obtained from the broadening parameter in Table II and Eq. (A1h), together with the condition $\hbar\Omega < \frac{1}{3}\Gamma$, provided the transverse mass $\mu_T \cong \mu_\parallel$ is known. From the value of the conduction-band transverse mass at $L$ given in Ref. 69, together with the equation of Ref. 73 and the critical-point data in Table II, $\vec{k}\cdot\vec{p}$ perturbation theory predicts $\mu_T \cong 0.086 m_e$ for this transition. Thus we calculate that field-induced broadening should begin to be observable at surface fields $\mathcal{E}_s \sim 30$ kV cm$^{-1}$. This value is in reasonable agreement with our experimental observations. Therefore, surface normal fields in the TER data of Ref. 25 are probably negligible.

The difference in asymmetry between the TER and Schottky-barrier ER line shapes in Fig. 3 is a result of the effect of the Ni film on the Seraphin coefficients,[74] which acts to modify the phase of the the complex Seraphin coefficient, $\tilde{C}_S$, in Eqs. (A3) in exactly the same manner as an increase in electron-hole interaction strength affects the complex coefficient $\tilde{C}_{ex}$. The extension of the complex Seraphin coefficient to describe $n$-phase laminar systems is straightforward and will be given elsewhere.[75] For a thin intermediate metallic phase of the thickness $d_m$ and dielectric function $\epsilon_m$ between a crystal described by $\epsilon = n^2$ and an ambient described by $\epsilon_a = n_a^2$, it can be shown that[75]

$$C_S \cong \frac{2n_a}{n(\epsilon-\epsilon_a)}\left(1+\frac{2i\omega d_m}{c}\,\frac{\epsilon_m-\epsilon_a}{\epsilon-\epsilon_a}\right), \qquad (3.2)$$

which, for typical metallic values for $\epsilon_m$ results in an extra phase shifts in $C_S$ which enhances the positive peak at the expense of the negative peak, exactly as an increase in the strength of the electron-hole interaction in the contact exciton approximation. This can be seen clearly in both $E_1$ and $E_1+\Delta_1$ transitions in Fig. 3.

We consider next the polarization effects seen in Fig. 3. In the low-field spectrum, a factor of 1.22±0.02 is sufficient to bring the spectra of the two principal orthogonal polarizations of the (110) surface into coincidence, except for a small discrepancy in the low-energy side of the $E_1$ structure. The high-field spectra show somewhat less

amplitude anisotropy than the low-field spectra, but show in addition a dependence of linewidth on polarization not present in the low-field results. The high-field anisotropies can be understood easily by the following qualitative arguments: Given the $\langle 111\rangle$ symmetry of the eight equivalent critical points contributing to the $E_1$ transition in the unperturbed crystal and the [110] direction of the applied field, the critical points divide into two groups: one consisting of the directions $\langle 1\bar{1}1\rangle$, $\langle 1\bar{1}\bar{1}\rangle$, $\langle \bar{1}\bar{1}1\rangle$, and $\langle \bar{1}1\bar{1}\rangle$, where the symmetry axis is perpendicular to the field, and the other consisting of the directions $\langle 111\rangle$, $\langle 11\bar{1}\rangle$, $\langle \bar{1}1\bar{1}\rangle$ and $\langle \bar{1}\bar{1}\bar{1}\rangle$, where the symmetry axis makes an angle of 35.3° to the field. Equations (A1) and (A3) of the Appendix show that the first, or perpendicular, group has a polarization dependence of the form $\frac{1}{3}(4+4\cos^2\theta)$, with $\mu_{\parallel}^{-1}=\mu_T^{-1}$, and the second has a polarization dependence $\frac{1}{3}(12-4\cos^2\theta)$, with $\mu_{\parallel}^{-1}=\frac{1}{3}\mu_T^{-1}+\frac{2}{3}\mu_L^{-1}$, where $\theta$ is the angle of the polarization vector measured with respect to $\langle 001\rangle$. Since $|\mu_L| \gg \mu_T$, the mass ratios show that the characteristic energy $\hbar\Omega$ is substantially larger for the perpendicular group than for the second, and thus the ER spectra from the first group should be larger and should show greater field-induced broadening than those from the second. From the polarization dependences, it is seen that the transitions in the perpendicular group contribute much more strongly for light polarized along [001]. This is in agreement with the results shown in Fig. 3. The fact that the high-field amplitude anisotropy is less than that for the low-field spectra is due to the saturation of the amplitude dependence of the electroreflectance response functions with increasing field. Thus the qualitative behavior of the high-field spectra can be explained completely within the classical generalized Franz–Keldysh theory.

The observed magnitude of the polarization anisotropy for low fields, $1.22\pm.02$, is substantially lower than the value predicted on the basis of a two-dimensional model in the low-field and effective-mass approximations. From Eq. (A5), for eight $\langle 111\rangle$ critical points in a [110] field, we find that

$$\frac{(\Delta R/R)_{[001]}}{(\Delta R/R)_{[1\bar{1}0]}}=\frac{4}{3}\,\frac{1+\mu_T/2\mu_L}{1+\mu_T/\mu_L} \qquad (3.3)$$

and thus the anisotropy ratio should approach 1.33. This discrepancy could be due to a finite value of $\mu_L$, measurements at a field value exceeding the low-field limit, deviations from the simple parabolic model, excitonic interactions, critical points being located slightly off the $\langle 111\rangle$ symmetry axes, or electric field effects on the momentum matrix element. The latter two effects have been proposed by Fischer[76] to explain similar anomalies in the TER spectra of the $E_1$ and $E_1+\Delta_1$ transitions in Ge. It is unlikely that either a finite value of $\mu_L$ or critical points off the $\langle 111\rangle$ symmetry axes provide the explanation. Equation (3.3) shows that a mass ratio $\mu_L/\mu_T=+17$ would be required to give the experimentally observed anisotropy ratio 1.22 for critical points on the symmetry axis, while an evaluation of the polarization factor in Eq. (A7) shows that it would be necessary to move ideal two-dimensional ($\mu_L=\infty$) critical points off the symmetry axes by 13° toward the $\langle 100\rangle$ axes in order to achieve the same result. We point out that the anisotropy ratio is a very slow ($\cos^2\theta$) function of the angle $\theta$ between the critical points and the symmetry axis, so that a substantial motion of the critical points off $\langle 111\rangle$ must occur before any effect is seen in the anisotropy (1% change for a 5° angle). Concerning the calculated mass ratio, the magnitude is reasonable but the sign is not, since it corresponds to an $M_0$ critical point and therefore implies an $M_1$ critical point at higher energy which is not seen. In order to investigate this further, room-temperature low-field measurements were performed and were found to yield an anisotropy ratio $1.32\pm0.03$, within experimental accuracy of the expected value. Since the broadening at room temperature was substantially higher ($\Gamma=61\pm3$ meV, $E_g=2921\pm5$ meV for the $E_1$ transition; $\Gamma=72\pm3$ meV, $E_g=3135\pm5$ meV for the $E_1+\Delta_1$ transition), "low-field" measurements could be made at higher applied fields at room temperature than at low temperatures. Since one would not expect matrix element effects to be particularly temperature dependent, the above results appear to rule out a strong contribution from this source. We believe the discrepancy is probably due to a combination of excitonic effects and deviations of the actual band structure from idealized parabolic models, both of which should become more important as the temperature is lowered.

The increased resolution obtainable with the Schottky-barrier technique enables us to resolve a large number of subsidiary oscillations of the $E_1+\Delta_1$ transition, as shown in the upper curve of Fig. 4. Also shown in Fig. 4 are the subsidiary oscillations of the $E_0+\Delta_0$ transition, taken under identical conditions. Since the $E_0+\Delta_0$ critical point is of type three-dimensional (3D) $M_0$ with a well-known reduced mass, this allows an independent estimate of the field magnitude to be obtained. The reduced mass of the $E_1+\Delta_1$ transition can also be obtained by comparing the oscillation period of these spectra with those of the $E_0+\Delta_0$ transition.

The asymptotic expressions describing the subsidiary oscillations are easily obtainable in closed form for one-dimensional (1D) and 3D $M_0$ critical points from the explicit analytic functions of the broadened Franz–Keldysh effect.[77] If $d=1$, 3 represents the dimension, then to within a multiplica-

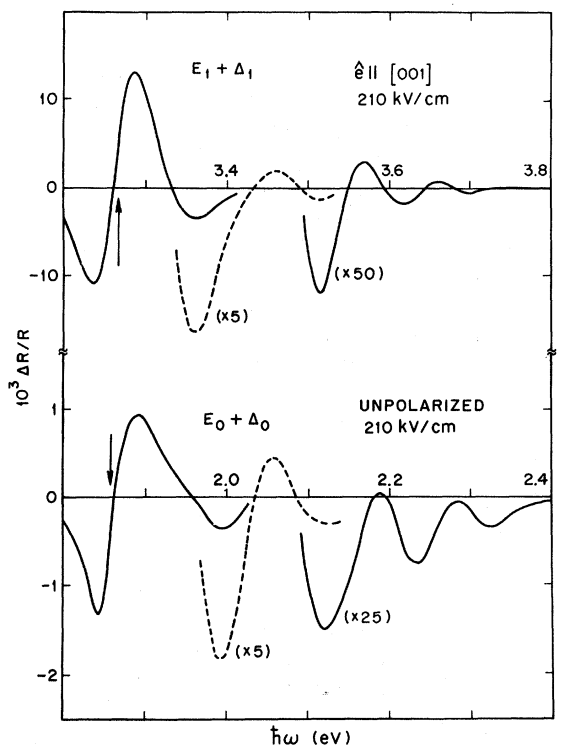


FIG. 4. Franz–Keldysh or subsidiary oscillations of the $E_0+\Delta_0$ (lower curve) and $E_1+\Delta_1$ (upper curve) transitions taken on the same sample under identical modulation conditions at 4.2 °K. The critical point energy is located by an arrow in each case.

tive constant the oscillations take the asymptotic form

$$\frac{\Delta R}{R} \sim (\hbar\omega - E_g)^{-(d+1)/4} \times \cos\left[\frac{2}{3}\left(\frac{\hbar\omega - E_g + i\Gamma}{\hbar\Omega}\right)^{3/2} - \frac{\pi}{4}(d-1)\right] \quad (3.4a)$$

$$\cong (\hbar\omega - E_g)^{-(d+1)/4} \exp\left(-\frac{\Gamma(\hbar\omega - E_g)^{1/2}}{(\hbar\Omega)^{3/2}}\right) \times \cos\left[\frac{2}{3}\left(\frac{\hbar\omega - E_g}{\hbar\Omega}\right)^{3/2} - \frac{\pi}{4}(d-1)\right] . \quad (3.4b)$$

We have not been able to verify this form explicitly for the 2D case ($d=2$), but by direct inspection of calculated curves[78] for a two-dimensional critical point it is seen that the subsidiary oscillations maintain the same period in the asymptotic limit, regardless of dimension. Surprisingly, the period appears to be maintained even in the presence of the Coulomb interaction, except for an increase in the period of the first several oscillations not described by the asymptotic expressions.[79] Thus, we take as a working model of the subsidiary oscillations the expression

$$\frac{\Delta R}{R} \sim (\hbar\omega - E_g)^{-1} \exp\left(-\frac{\Gamma(\hbar\omega - E_g)^{1/2}}{(\hbar\Omega)^{3/2}}\right) \times \cos\left[\theta + \frac{2}{3}\left(\frac{\hbar\omega - E_g}{\hbar\Omega}\right)^{3/2}\right] , \quad (3.5)$$

where $\theta$ is a phase factor depending on electron-hole interaction strength, dimensionality, and short-range scattering processes. Let $[(\Delta R/R)_\nu, E_\nu]$ represent the amplitude and energy position of the $\nu$th extremum of the sequence of subsidiary oscillations. Since successive extrema represent a change of $\pi$ in the argument of the cosine term, we may write

$$\nu\pi = \theta + \tfrac{2}{3}\left[(\hbar\omega - E_g)_\nu/\hbar\Omega\right]^{3/2} , \quad (3.6)$$

where the phase factor $\theta$ and characteristic energy $\hbar\Omega$ can be obtained from the intercept and slope, respectively, of a plot of $(\hbar\omega - E_g)_\nu^{3/2}$ vs $\nu$. The resulting value of $\hbar\Omega$ defines a relationship between field magnitude and reduced mass. A second condition is obtained via the attenuation of the peak amplitudes. From Eq. (3.5),

$$\ln\left[(\hbar\omega - E_g)_\nu (\Delta R/R)_\nu\right] = -\Gamma\left[(\hbar\omega - E_g)^{1/2}\right]_\nu/(\hbar\Omega)^{3/2} . \quad (3.7)$$

Therefore, a plot of $\ln[(\hbar\omega - E_g)_\nu (\Delta R/R)_\nu]$ vs $[(\hbar\omega - E_g)^{1/2}]_\nu$ yields a relationship between $\Gamma$ and $\Omega$.

Figure 5 shows the results of plotting our data in the manner described above, for both the $E_0 + \Delta_0$ and the $E_1+\Delta_1$ transitions. In all four cases,

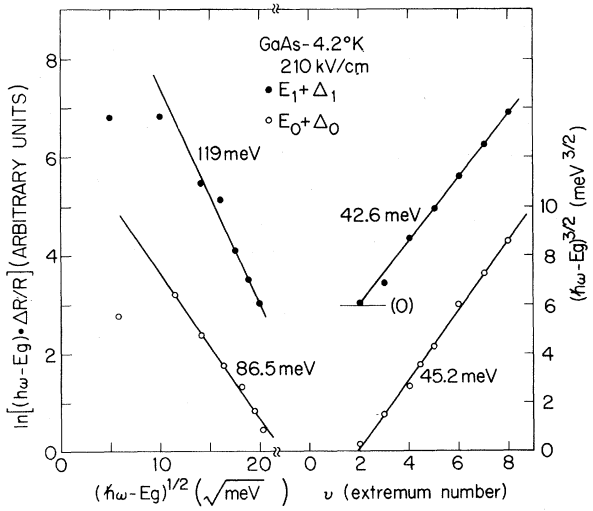


FIG. 5. Fit of the asymptotic form of the Franz–Keldysh oscillations, given by Eq. (3.5), to the experimental data of Fig. 4. Right side: $(\hbar\omega - E_g)^{3/2}$ vs $\nu$, index number of local extrema. Note zero offset for $E_1+\Delta_1$ data. Energies given refer to values of $\hbar\Omega$ determined from the slopes of the straight lines. Left side: $\ln[(\hbar\omega - E_g)\Delta R/R]$ vs $(\hbar\omega - E_g)^{1/2}$. Ordinate zero is arbitrary. Energies given refer to values of $\Gamma$ determined from the slopes of the straight lines.

very good straight-line fits are obtained with the exception of the first several points, where excitonic effects are presumably strong and there also exists some interference from the subsidiary oscillations of the $E_0$ and $E_1$ transitions. The polarization direction for the $E_1+\Delta_1$ spectrum was chosen in order to maximize the contribution from the four equivalent critical points perpendicular to the field. Since $\hbar\Omega$ is significantly less for these critical points, they are expected to dominate, particularly in the region of the subsidiary oscillations. The absence of irregularities in amplitude and peak position indicates that this is the case.

The slope of the right-hand curves in Fig. 5 yields 45.2±1 and 42.6±1 meV for $\hbar\Omega$ for the $E_0+\Delta_0$ and $E_1+\Delta_1$ transitions, respectively. Using the value $\mu_{\parallel so}=0.046m_e$,[64] we calculate from the former value that $\mathcal{E}_s=210$ kV cm$^{-1}$. This compares well with the value, $\mathcal{E}_s=196$ kV cm$^{-1}$, estimated from the period of the interference oscillations in Fig. 2, and is substantially larger than the value, $\mathcal{E}_s=130$ kV cm$^{-1}$ obtained by using the smaller value of $N_D$ calculated from high-frequency capacitance measurements, as was anticipated in Sec. II C.

The value of the reduced mass of the $E_1+\Delta_1$ transition can be obtained independently of the field from Eq. (A1h) by calculating the cube of the ratio of the two values of $\hbar\Omega$ obtained in Fig. 5 and using the known mass, $\mu_{so}=0.046m_e$, of the $E_0+\Delta_0$ transition. We find

$$(\mu_T)_{E_1+\Delta_1}/\mu_{so}=1.195\pm0.18\ , \tag{3.8a}$$

$$(\mu_T)_{E_1+\Delta_1}=(0.055\pm0.008)m_e\ . \tag{3.8b}$$

This value is about 30% below the value of $0.086m_e$ estimated from $\vec{k}\cdot\vec{p}$ theory.[73]

This discrepancy cannot be resolved completely at this stage. We believe the most likely explanation is that the $\vec{k}\cdot\vec{p}$ theory is not exact. Interactions with higher bands are ignored in the theoretical expression,[73] which suggests that the $\vec{k}\cdot\vec{p}$ mass should be considered only as an approximation. However, alternative explanations which should be considered include nonparabolicity and Coulomb effects. For instance, nonparabolicity effects may reduce the band curvature at several hundred meV above both critical point and thus raise the value of *both* masses, bringing the ratio into better agreement. Nonparabolicity effects along the longitudinal symmetry axis may also substantially alter Eq. (3.5), particularly with respect to the amplitude dependence of the subsidiary oscillations, which might be expected to decay faster for nonparabolic bands. There is some experimental evidence for this effect: If Eq. (3.7) is used to calculate $\Gamma$ from the slope of the lines in Fig. 5, we find $\Gamma=86.5$ and 119 meV for the $E_0+\Delta_0$ and $E_1+\Delta_1$ transitions, respectively. These values are far in excess of the values, $\Gamma=6\pm2$ meV and $\Gamma=38$ meV, obtained from low-field electroreflectance analysis, thus suggesting that the theory is lacking in some important detail. Field inhomogeneity effects do not appear to be the cause; an application of inhomogeneous perturbation theory[9] to a linear field profile appropriate to this crystal (depletion depth 1 $\mu$m) using Eq. (3.5) to describe $\Delta R/R$ yielded at most a few percent increased in attenuation rate with parameters from Table II. Another alternative lies in the possible dependence of the phase factor $\theta$ in Eq. (3.5) upon field and photon energy. The long-range scattering property of the Coulomb potential could combine with band nonparabolicity effects to produce a variable phase factor. It is expected that the envelope of the oscillations would be much more sensitive to these effects than the period. The present theory is not adequate to resolve these questions.

### C. $E_0'$, $E_2$ Transitions

Typical spectra in the energy range 4.2–5.6 eV, which contains the $E_0'$ and $E_2$ transitions, are shown in Fig. 6. The upper curves represent low-field spectra for the two principal polarization directions. The lower spectra were taken at relatively high values of the surface field. All data in Fig. 6 correspond to a temperature of 4.2°K.

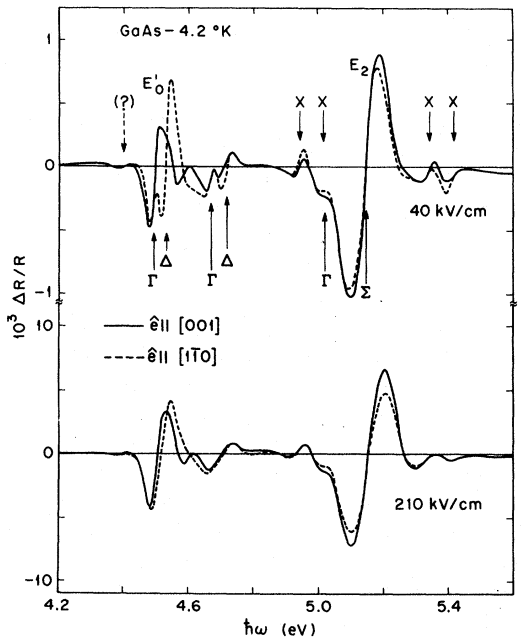


FIG. 6. Schottky-barrier ER spectra for GaAs at 4.2 °K, taken at low and relatively high values of the surface field in the energy range of the $E_0'$ and $E_2$ transitions, for the two principal polarizations on the (110) surface. The energies of the critical points of symmetries shown are obtained as discussed in the text.

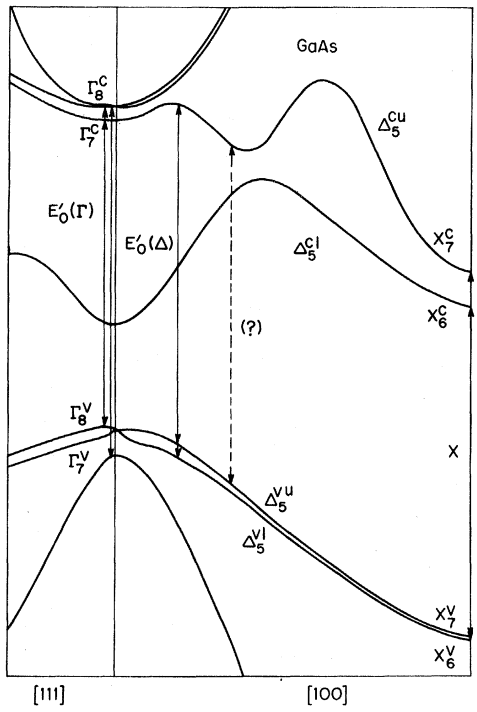


FIG. 7. Approximate band structure for GaAs (after Ref. 69), showing the proposed location of critical points giving rise to the low-field structure of Fig. 6. The effect of the $k$-linear terms near $k=0$ has been exaggerated for clarity.

We discuss first the $E_0'$ transitions near 4.5, 4.7, and 5.0 eV. It is generally accepted that these transitions are due to critical points at or near the center of the Brillouin zone, between the spin-orbit-split upper valence band and the spin-orbit-split second conduction band. Before proceeding further, we emphasize that both the upper valence- and upper conduction-band pairs involved in these transitions are degenerate at $k=0$, with terms linear in $k$ being present due to the lack of inversion symmetry of the crystal[80] (see Fig. 7). Thus, critical points in the vicinity of the zone center are expected to be relatively complicated, and any analysis in terms of simple parabolic models must necessarily be approximate. Nevertheless, the low-field data in Fig. 6 represent over an order-of-magnitude improvement in resolution as compared to previous work, which enables us to obtain some new and definitive conclusions about these transitions despite the use of approximate model densities of states.

The general conclusions can be summarized as follows: First, at very low values of the field, the lower two members of the $E_0'$ triplet are each observed to consist of two distinct transitions. These are the pairs labeled $\Gamma$ and $\Delta$ in Fig. 6, for reasons which will be discussed shortly. This result is significant, for Rehn and Kyser[33] recently observed $\Delta$ symmetry behavior in TER measurements on the $E_0'$ transitions of GaAs, but were unable to resolve the separate $\Gamma$ components and hence postulated that the entire $E_0'$ structure was of $\Delta$ origin. The Rehn–Kyser interpretation conflicted with energy band theory, where contributions of $\Gamma$ symmetry are also expected, and also with measurements of the $E_0'$ transitions of Ge, where only $\Gamma$ contributions are observed.[8,76] The observation of the doublet nature of these transitions resolves the discrepancy. Secondly, by comparing the low- and high-field spectra, we are able to obtain the approximate *location* of the $\Delta$ critical points along $\langle 001\rangle$ axes, showing that they occur away from $\Gamma$ by about 10% of the $\Gamma - X$ separation. Thirdly, the $\Delta$ component is observed to vanish in the lowest transition for light polarized in the [001] direction. This is not due to an optical selection rule, as is usually the case in optical spectroscopy, but instead is due to the vanishing of the ER response of a hyperbolic critical point when the field is oriented along an infinite-mass direction. This effect had been predicted in the generalized theory of the Franz–Keldysh effect[77,81] but has never been previously observed.

We consider first the symmetry assignment for the transitions in the $E_0'$ triplet based on the polarization dependence in Fig. 6, and the general result Eq. (A7). The transitions labeled $\Gamma$ show virtually no polarization dependence, as expected for a single isotropic critical point, with the possible exception of the transition near 5 eV for reasons discussed below. Fischer and Bottka[82] also report no polarization effects in surface-barrier ER measurements on the $E_0$ transition of Ge, which also involves a degenerate valence band. We therefore assign these transitions to the zone center, as indicated in Fig. 7. The $k$-linear terms will move these critical points off $\Gamma$ to locations along the $\langle 111\rangle$ symmetry axes,[80] as indicated schematically, but this effect is expected to be small. The critical point energies and broadening parameters for these transitions can be obtained from the low-field spectra by means of the curve-fitting analysis discussed in connection with the $E_1$ transitions. The results are summarized in Table II. Since the band structure is complicated, nonparabolicity effects probably influence the values obtained. Note, for instance, that the broadening parameter for the lowest $\Gamma$ transition is substantially larger than that for the intermediate $\Gamma$ transition, contrary to expectations based on recombination probabilities of excited states of similar symmetries. Note also that this is the *only* allowed $\Gamma$ transition to the nondegenerate second conduction band, which is also the only conduction band which reverses its curvature at $k=0$, exhibiting a maximum rather

near the zone center. Band nonparabolicity due to two nearly confluent critical points of this type always widens the resonant line shape,[53] making the broadening appear larger than it actually is. Thus, the value of $\Gamma$ for the lowest $E_0'$ transitions (both $\Gamma$ and $\Delta$) should be regarded as upper limits only. (The error limits on these specific numbers refer only to the curve-fitting procedures.) We note that the critical point energies themselves are probably determined fairly accurately, since the broadening introduced by the nonparabolicity tends to be symmetric. The spin-orbit splittings at $\Gamma$ can thus be obtained, and we find for the upper conduction band, $\Delta_0' = 171 \pm 15$ meV, and for the valence band, $\Delta_0 = 355 \pm 20$ meV. The latter number is somewhat larger than the more accurate value, $341 \pm 2$ meV, obtained from direct measurements of the $E_0$ and $E_0 + \Delta_0$ transitions, a discrepancy which is due to the overlap of the second transition at $X$ ($X_6^v - X_7^c$; see below). The generally good agreement of the valence-band spin-orbit splittings tends to support the symmetry identification of these transitions, as does the general 4:2:1 amplitude decrease with increasing energy, which is also seen for Ge.[8]

We consider next the transitions labeled $\Delta$ in Fig. 6, which are characterized by a polarization dependence so strong that the lower $\Delta$ transition is completely absent for light polarized parallel to the [001] direction. The symmetry analysis can be performed with the help of Eq. (A7). We consider only the high-symmetry critical points of type {100}, {110}, and {111}, since it is unlikely that such strong polarization effects could be achieved at points of lower symmetry. Assuming a single (positive) transverse mass component $\mu_T$ and a longitudinal component $\mu_L$, we find for a surface-barrier ER measurement on the (110) surface where $\hat{g} = (\hat{x} + \hat{y})/\sqrt{2}$ and $\hat{n} = [(\hat{x} - \hat{y})/\sqrt{2}]\sin\theta + \hat{z} \times \cos\theta$ that the change in reflectivity, $\Delta R/R$, will have the polarization dependences

$$\left(\frac{\Delta R}{R}\right)_{\langle 100\rangle} \sim \frac{1}{\mu_T}(1-\cos 2\theta) + \frac{1}{2}\left(\frac{1}{\mu_T}+\frac{1}{\mu_L}\right)(3+\cos 2\theta)\,, \quad (3.9a)$$

$$\left(\frac{\Delta R}{R}\right)_{\langle 110\rangle} \sim \frac{2}{\mu_L}+\frac{1}{\mu_T}(1+\cos\theta) + \frac{1}{8}\left(\frac{3}{\mu_T}+\frac{1}{\mu_L}\right)(5-\cos 2\theta)\,, \quad (3.9b)$$

$$\left(\frac{\Delta R}{R}\right)_{\langle 111\rangle} \sim \frac{2}{3\mu_T}(3+\cos 2\theta) + \frac{2}{9}\left(\frac{1}{\mu_T}+\frac{2}{\mu_L}\right)(5-\cos 2\theta)\,, \quad (3.9c)$$

for $\langle 100\rangle$, $\langle 110\rangle$, and $\langle 111\rangle$ critical points, respectively. Note that in *no* case will $\Delta R/R$ vanish, for any value of $\theta$, unless $\mu_L < 0$ ($M_1$ critical point). Thus, a vanishing structure cannot be due entirely to optical selection rules, but rather to a specific value of the reduced-mass ratio $\mu_L/\mu_T$, and then only if this ratio is negative. This is a purely ER effect due to the requirement that the effective mass appropriate to any critical point is that value calculated in the direction of the electric field.[77,81]

The mass ratios which cause the spectra to vanish for [001] polarization, in agreement with experiment, are $\mu_L/\mu_T = -1$, $-\frac{5}{7}$, and $-\frac{1}{2}$ for $\langle 100\rangle$, $\langle 110\rangle$, and $\langle 111\rangle$ critical points, respectively. Note it is not possible to make a unique symmetry identification on the basis of polarization measurements, as proven in Sec. IID. Accordingly, we base the $\Delta$ symmetry assignment on two experimental data: the TER measurements of Rehn and Kyser,[33] and the fact that, of the three symmetries investigated above, the $\Delta$ critical points result in a vanishing spectrum for [001] polarization with the largest value of the (negative) longitudinal mass. The additional symmetry information available in the TER measurement, which can in principle determine all three fourth-rank tensor coefficients, is perhaps the strongest experimental evidence in favor of this assignment. Band-structure calculations[27,69] also favor a $\Delta$ assignment, providing a series of possible locations for $\langle 100\rangle$ critical points of these approximate energies. These include the point of inversion of the singly degenerate $\Delta_5^{cu}$ second conduction band very near to $k = 0$, indicated in Fig. 7, a possible pair of critical points of type $M_0$ near the pseudocrossing of the $\Delta_5^c$ conduction bands about one-third of the way from $\Gamma$ to $X$, and the transitions at the $X$ point themselves.

The behavior of the $\Gamma$-$\Delta$ pairs at high fields indicates that the critical points giving rise to the $\Delta$ structures are actually located very close to the zone center, of the order of 10% of the distance from $\Gamma$ to $X$. We obtain this result by the following argument. As the field is increased, the $\Gamma - \Delta$ pairs begin to merge in the experimental spectra. At a field of $\sim 200$ kV cm$^{-1}$, the $\Gamma$-$\Delta$ pairs have completely lost their individual identity and appear as shown in the lower curves in Fig. 6. Note that there is no indication of two critical points in each structure at these fields, and that the polarization dependence which remains lies between that of the individual $\Gamma$ and $\Delta$ structures, suggesting a weaker $\Delta$ symmetry. Thus at high fields the simple parabolic models for the individual $\Gamma$ and $\Delta$ transitions have broken down completely. The simple parabolic models are expected to fail if the electron momentum under acceleration by the field can change sufficiently within a scattering lifetime $\tau = \hbar/\Gamma$ so that the electron can scatter through

both critical points. Since $F = e\mathcal{E} = \hbar\Delta K/\Delta T$ we calculate for $\mathcal{E} = 200$ kV cm$^{-1}$, $\Gamma = 30$ meV, that

$$\Delta k/k_L = e\mathcal{E}a_0/2\pi\Gamma = 0.06 \ , \qquad (3.10)$$

where $k_L = 2\pi/a_0$ is the length from $\Gamma$ to $X$ in the Brillouin zone. Thus we conclude that the $\Gamma$-$\Delta$ critical point separation is of the order of 10% of the $\Gamma - X$ distance, which indicates the $\Delta$ critical points giving rise to the $\Delta$ structures in Fig. 6, are near or part of the complicated band structure near $\Gamma$. The strong polarization dependence of the $\Delta$ transitions is characteristic of a hyperbolic critical point, which further suggests that these structures are due to $M_1$ critical points between the nondegenerate second conduction band and the light- and heavy-hole valence bands, located at the inversion point of the second conduction band (see Fig. 1 of Ref. 69). The interpretation also correlates well with the results of Ref. 27, where an $M_1$ critical point is predicted along $\Delta$ 20% of the way from $\Gamma$ to $X$. However, this interpretation does contain some inconsistencies, namely, the longitudinal mass of the higher-energy critical point must be formed with the light-hole band and therefore should be smaller, so the polarization dependence of the higher-energy $\Delta$ transition should be stronger, contrary to experiment. Nevertheless, an improved treatment would depend on a detailed calculation of the band structure near $\Gamma$, together with a complete treatment by either the low-field or the Franz–Keldysh theories for the nonparabolic band structure which results. Nevertheless, the general conclusion of adjacent pairs of $\Gamma$-$\Delta$ critical points appears to be supported well even by qualitative arguments. The assignment of the $\Delta$ transitions to the pseudocrossing point by Rehn and Kyser[33] is difficult to justify for a number of reasons: It is not clear that a critical point is formed here in the case of the lower conduction band, due to the apparently monotonic increase in the valence-conduction interband energy from $\Gamma$ to $X$ for this band.[69] Also, a critical point formed by the upper band would be an $M_0$ critical point which would not have the strong polarization dependence seen in the low-field spectrum. We mention that the extremely weak structure in Fig. 6 at 4.4 eV correlates well with the predicted[27] energy of the pseudocrossing $M_0$ critical point to the upper valence band, if all energies are shifted to bring the $M_1$ critical point in Ref. 27 into agreement with experiment.

A number of additional structures also appear in the spectra of Fig. 6. We emphasize again that the surface-barrier configuration cannot provide sufficient information for a unique determination of symmetry from polarization measurements alone, so the assignments which follow are made primarily on the basis of energy separations and consistency of polarization anisotropy. These assignments can, however, be examined by means of Schottky-barrier piezoreflectance measurements. The $E_2$ transition centered about 5137 eV dominates the spectrum and includes contributions from large regions of the Brillouin zone. The polarization dependence of this structure is weak and opposite to that of the $\Delta$ transitions, consistent with a $\Sigma$ symmetry assignment using reasonable values of $\mu_L$ and $\mu_T$ in Eq. (A7). Both the magnitude of the structure and its anomalously large broadening parameter, over twice those of transitions at equivalent energies, give direct evidence of contributions from extended regions of the Brillouin zone.

Four transitions in the upper curve of Fig. 6 are identified with the transitions between the valence and conduction bands at the $X$ point, where both valence and conduction bands are split by the antisymmetric potential. One of these transitions is superimposed on the uppermost $\Gamma$ transition of the $E_0'$ triplet. These transitions are all of the same order of magnitude, have essentially the same values of the broadening parameter, and, more important, occur in pairs where the splittings within each pair are virtually equal. These structures give the splitting of the valence bands at $X$ as $\Delta_2 = 77 \pm 10$ meV. The splitting of the conduction bands at $X$ is therefore found to be $\Delta_2' = 402 \pm 10$ meV. Besides the characteristic quadruplet pattern, the polarization anisotropy of these transitions is compatible with $\Delta$ symmetry if the longitudinal mass is fairly large. This assignment is further supported by Rowe and Christman,[34] whose photoemission measurements indicate the onset of $X_7^v \rightarrow X_6^c$ transitions in the vicinity of 4.9 eV at room temperature.

## IV. DISCUSSION

The main spectroscopic results of this paper are summarized in Table II, together with data previously obtained with other modulation techniques. In general, we have been able to determine known critical point energies and broadening parameters to a much higher degree of accuracy through the use of the low-temperature Schottky-barrier ER technique[8] and by curve-fitting to simple low-field model line shapes.[54] We have also been able to determine these parameters for a series of transitions which have not been resolved previously by any technique.

It is of interest to compare our results with previous experimental work on GaAs. We have already mentioned that the WDR technique of Sell[36,37] is comparable to the Schottky-barrier ER technique at the $E_0$ transition. This is due to the extremely small lifetime broadening of the transition, and the fact that the dominant electric field

effect here is the modulation of the $n=1$ discrete exciton line by means of the optical mismatch between the bulk and the space-charge region. Thus, both the Schottky-barrier ER and the WDR techniques are observing the same effect at the $E_0$ transition. The thermoreflectance (TR) results of Matatagui *et al.*[22] at the $E_0$ transition do not compare in accuracy to either the Schottky-barrier ER or the WDR measurements.

Numerous experimental measurements have been made to determine the critical point energies of the $E_1$ and $E_1+\Delta_1$ transitions. Here, the most accurate determination of critical point energies is obtained by analysis of ER data. We note here that essentially the same values of the critical point energies and broadening parameters are obtained from either the Schottky-barrier ER data reported here or the TER data previously obtained by Kyser and Rehn.[25] This proves that the normal surface fields were negligibly small in the TER experiment, which indicates that there is nothing in principle to prevent equally accurate spectroscopic measurements to be made with TER, a geometry which also has the added advantage that all three independent complex tensor coefficients of $\chi^{(3)}(\omega;0,0,\omega)$ can be determined. The TR[22] and wavelength-modulated reflectance (WMR)[26,32] data in Table II refer to energies of reflectivity or modulated reflectivity peaks, and not to energies of the critical points responsible for these transitions. The amount of structure present in these first-derivative line shapes is insufficient to enable the broadening parameters to be determined easily from the experimental data without additional differentiation,[83] in contrast to ER spectra where the lifetime broadening is simply related to the energy separation of the extrema in the third-derivative spectral line shape.[53,54]

At sufficiently high fields, a series of subsidiary oscillations is observed to extend about 0.5 eV to higher energy above the $E_1+\Delta_1$ transition. From a comparison of the period of the oscillations of these transitions with those observed for the $E_0+\Delta_0$ transitions under identical experimental conditions, we have obtained the first determination of the transverse mass of the $E_1+\Delta_1$ transitions in GaAs, finding $\mu_T=(0.055\pm0.008)m_e$.

Table II illustrates the resolution improvement obtained with the Schottky-barrier ER technique above the $E_1+\Delta_1$ transitions. The low-field ER measurements reported here resolve for the first time separate $\Gamma$ and $\Delta$ critical points in the $E_0'$ triplet, and in addition resolve the quadruplet at $X$ in the $E_2$ complex. The capability of determining broadening parameters also demonstrates conclusively that the lowest $\Gamma$ transition of the $E_0'$ triplet, and the peak $E_2$ structure, are not due to simple parabolic critical points because these transitions are anomalously broad compared to others in the same energy range. The separation of the $\Gamma$ and $\Delta$ components in low-field spectra of the $E_0'$ transitions allows us to determine the spin-orbit splitting at $\Gamma$, which is $\Delta_0'=171\pm15$ meV. This splitting is somewhat smaller than the value at $\Delta$, which is $\Delta_0''=183\pm15$ meV. Since the $\Delta$ critical points are in close proximity to the zone center, at high fields the $\Gamma$-$\Delta$ pairs merge and the spin-orbit splitting becomes more nearly the $\Delta$ value. The resolution of the individual members of the $X$ quadruplet also allows us to resolve the splittings of the valence and conduction bands at $X$ under the action of the spin-orbit splitting and the antisymmetric potential. We find these values to be $\Delta_2=77\pm10$ meV and $\Delta_2'=402\pm10$ meV, respectively. The splitting of the upper conduction band is appreciably less than the commonly accepted photoemission value of $580\pm50$ meV.[19,20] Our value of the $X_7^v\rightarrow X_6^c$ energy separation 4938 $\pm10$ meV is in excellent agreement with the value $4.9\pm0.1$ meV obtained by Rowe and Christman[34] from a reevaluation of these photoemission results. Finally, it is worth noting that the $X_6^c\rightarrow X_7^c$ energy separation $402\pm10$ meV is also in excellent agreement with the value 0.43 eV obtained in 1962 by Greenaway[15] from an analysis of early reflectivity data for GaAs.

Our measurements can also be compared to energy band structure calculations for GaAs. The most recent calculation by Zucca *et al.*[27] using the empirical pseudopotential method yields results which are, in fact, quite close to our values except for being consistently low by about 200 meV. Of particular interest in this calculation is the prediction of $M_1$ critical points of $\Delta$ symmetry at 4.38 and 4.55 eV, about 20% of the way from $\Gamma$ to $X$, which presumably could correspond to the $\Delta$ structures which we observe at 4.53 and 4.71 eV, respectively. It is of some interest to speculate that the $M_0$ transition predicted to be at 4.23 eV by this calculation may be responsible for the very weak structure which we observe near 4.4 eV, below the onset of the lowest member of the $E_0'$ triplet. However, no values of the critical point energies at $\Gamma$ or at $X$ obtained in this calculation have been published, so it is not possible at present to comment further on this calculation.

The band-structure calculations by Herman *et al.*[71] show excellent agreement at $\Gamma$ ($\Gamma_{15}^c=4.6$ eV; weighted experimental value with spin-orbit splitting removed = 4.603 eV) but show a substantially smaller band separation at $X(X_5^v\rightarrow X_1^c=4.21$ eV; weighted experimental value with splitting removed = 4.956 eV). The reasons for the relatively large discrepancy at $X$ are not clear. Also, the calculations as given are not sufficiently detailed to determine whether pairs of $\Gamma$-$\Delta$ critical points

near the zone center, as seen by experiment, are present in this band structure.

The $\vec{k}\cdot\vec{p}$ calculations of Pollak *et al.*[69] show the existence of the $M_1$ critical points of $\Delta$ symmetry very near the center of the Brillouin zone. The energy separation, 0.18 eV, is in excellent agreement with our observations, but the actual separation of these critical points is too low by about 130 meV. The calculated $X_7^v$-$X_6^c$ energy separation is significantly lower (4.36 eV) than our results indicate (4.938 eV). Also, the $X_6^c$-$X_7^c$ splitting appears to be much too large, although no numerical values are quoted.

We mention that the spin-orbit splittings $\Delta_0 = 0.34$ eV, $\Delta_0' = 0.19$ eV, and $\Delta_2 = 0.09$ eV calculated by Wepfer *et al.*[84] by means of a relativistic orthogonalized plane wave formalism using the Kohn-Sham–Gaspar exchange are in excellent agreement with our values of 341, 171, and 77 meV, respectively, for these quantities. This suggests that the theoretical values[84] should be accurate enough to be useful in identifying the symmetry of transitions in other materials on the basis of energy separations.

Finally, we have found the Schottky-barrier technique to be extremely useful in applications to other materials as well. The previous work on Ge[8] has already been mentioned. Measurements on Si have yielded the first direct observation of the $E_0$ and $E_0+\Delta_0$ transitions in Si, at threshold energies of $4185\pm10$ and $4229\pm10$ meV, respectively.[85] If ER spectra are intended only for the measurement of threshold energies and broadening parameters, it is even possible to relax the restriction of forming a fully depleted Schottky barrier, and to make measurements on systems which simply form nonohmic contacts. We have performed measurements of this type on materials such as epitaxilly grown GeSi alloys[86] and pseudobinary alloy films such as $Ga_xAl_{1-x}As$. It therefore appears that the Schottky-barrier configuration should be applicable to a large class of materials.

## ACKNOWLEDGMENTS

The authors wish to express their appreciation to J. E. Rowe, E. O. Kane, and D. D. Sell for discussions concerning this work.

## APPENDIX: THEORY

In this Appendix, we list equations and define quantities used at various points in the text. We consider only the one-electron theory[77,81,87] and its low-field (third-derivative or resonant quadratic electro-optic) limit,[4–6] as extended by the treatment of electron-hole correlation effects in the contact-exciton approximation.[88] All expressions assume a single valence-conduction-band pair, denoted where necessary by the subscripts $v$ and $c$, respectively.

(i) General expression for the field-induced change in dielectric function, intermediate-field case (Franz–Keldysh theory)[5,87]:

$$\Delta\epsilon_{ij}(\hbar\omega,\vec{\mathcal{E}}) = \epsilon_{ij}(\hbar\omega,\vec{\mathcal{E}}) - \epsilon_{ij}(\hbar\omega)$$

$$= \frac{ie^2\hbar^2}{\pi^2 m^2 E_+^2}\int_{BZ} d^3k\, P_{vc}^i(\vec{k})\, P_{cv}^j(\vec{k}) \times\int_0^\infty du\,\left(e^{-iu^3(\hbar\Omega)^3/3}-1\right) e^{iu[E_+ - E_{cv}(\vec{k})]} \qquad \text{(A1a)}$$

$$= \frac{e^2\hbar^2}{\pi m^2 E_+^2}\int_{BZ} d^3k\, P_{vc}^i(\vec{k})\, P_{cv}^j(\vec{k}) \times\left[\frac{1}{\hbar\Omega}\,\mathrm{Gi}\left(\frac{E_{cv}(\vec{k})-E_+}{\hbar\Omega}\right) + \frac{i}{|\hbar\Omega|}\,\mathrm{Ai}\left(\frac{E_{cv}(\vec{k})-E_+}{\hbar\Omega}\right) - \frac{1}{E_{cv}(\vec{k})-E_+}\right], \qquad \text{(A1b)}$$

where

$$\vec{P}_{cv}(\vec{k}) = \langle c\,\vec{k}|\,\vec{p}\,|\,v\vec{k}\rangle\ , \qquad \text{(A1c)}$$

$$E_+ = \hbar\omega + i\Gamma\ , \qquad \text{(A1d)}$$

$$E_{cv}(\vec{k}) = E_c(\vec{k}) - E_v(\vec{k})\ , \qquad \text{(A1e)}$$

$$(\hbar\Omega)^3 = \tfrac{1}{8}e^2(\vec{\mathcal{E}}\cdot\nabla_{\vec{k}})^2 E_{cv}(\vec{k}) \qquad \text{(A1f)}$$

$$= \tfrac{1}{8}(e^2\hbar^2)\mathcal{E}_i\mathcal{E}_j[\mu_{cv}(\vec{k})]_{ij}^{-1} \qquad \text{(A1g)}$$

$$= e^2\mathcal{E}^2\hbar^2/8\mu_\parallel\ . \qquad \text{(A1h)}$$

In Eqs. (A1), BZ refers to integration over the Brillouin zone, $\vec{P}_{cv}(\vec{k})$ is the momentum matrix element between the band $c$ and $v$ at the point $\vec{k}$, $\hbar\omega$ is the photon energy, $\Gamma$ is the phenomenological broadening parameter, $E_{cv}(\vec{k})$ is the interband energy, and $\hbar\Omega$ is the characteristic electro-optic energy expressed in terms of the externally applied electric field $\vec{\mathcal{E}}$ and the second-rank reciprointerband reduced mass tensor $[\mu_{cv}(\vec{k})]^{-1}$. This tensor has the scalar value $1/\mu_\parallel$ in the field direction. Ai($z$) and Gi($z$) are Airy functions of complex argument. Summation over repeated tensor indices, as in Eq. (Alg), is implied throughout.

(ii) General expression for the field-induced change in the dielectric function, low-field case[4,6]:

$$\lim_{\vec{\mathcal{E}}\to 0}\Delta\epsilon_{ij}(\hbar\omega,\vec{\mathcal{E}}) = \frac{2e^2\hbar^2}{\pi^2 m^2 E_+^2}\int_{BZ} d^3k\, P_{vc}^i(\vec{k})\, P_{cv}^j(\vec{k})\,\frac{(\hbar\Omega)^3}{[E_{cv}(\vec{k})-E_+]^4} \qquad \text{(A2a)}$$

$$= 4\pi\mathcal{E}_k\mathcal{E}_l\,\chi_{ijkl}(\hbar\omega)\ , \qquad \text{(A2b)}$$

where

$$\chi_{ijkl}(\hbar\omega) = \frac{e^4\hbar^4}{16\pi^3 m^2 E_+^2}\int_{BZ} d^3k$$

$$\times \frac{P^i_{vc}(\vec{k})\,P^j_{cv}(\vec{k})\,[\mu_{cv}(\vec{k})^{-1}]_{kl}}{[E_{cv}(\vec{k})-E_+]^4} \quad . \tag{A2c}$$

The quantity $\chi_{ijkl}$ is the complex fourth-rank quadratic nonlinear optical electroreflectance tensor, whose line shape is related to the third derivative of the unperturbed dielectric function.

(iii) General expression relating the field-induced change in the dielectric function to the experimentally measured relative reflectivity change $\Delta R/R$[53,54]:

$$\Delta R/R = \mathrm{Re}\,[\tilde{C}\,n_i n_j\,\Delta\epsilon_{ij}(\hbar\omega, \vec{\mathcal{E}})] \quad , \tag{A3a}$$

where $\hat{n}$ is the unit polarization vector of the incident radiation. The quantity $\tilde{C}$ is a product of complex functions, each weakly dependent on $\hbar\omega$:

$$\tilde{C} = C_S\,C_{ex}\,C_{in} \, , \tag{A3b}$$

where[9,75,88]

$$C_S = \alpha - i\beta$$

$$= 2n_a/n(\epsilon-\epsilon_a) \quad , \tag{A3c}$$

$$n^2=\epsilon, \quad n_a^2=\epsilon_a \quad , \tag{A3d}$$

$$C_{ex}=[1-g(\epsilon-1)]^2 \quad , \tag{A3e}$$

$$g=-m^2P^2(\hbar\omega)^2/(4\pi^2e^2\hbar^2) \quad , \tag{A3f}$$

$$C_{in}=-2iK\int_{-\infty}^{0}dz\,e^{-2ikz}[\mathcal{E}(z)/\mathcal{E}(0)]^2. \tag{A3g}$$

Here, $P$ is the average momentum matrix element and $K$ is the propagation vector of light in the solid. These expressions assume a scalar unperturbed dielectric function, $\epsilon$. The subscript $a$ refers to the ambient phase. The function $C_S$ represents the Seraphin coefficients[74] $\alpha$ and $\beta$ for a two-phase system of solid and ambient, and it depends only on the optical properties of the system. The function $C_{ex}$ represents electron-hole effects in the contact-exciton approximation.[88] The function $C_{in}$ represents the effect of nonuniform modulating field[9] in a solid extending to $z\le 0$; $\mathcal{E}(0)$ is the value of the surface field. Equation (A3g) is the simplified form appropriate to the low-field equations (A2).

(iv) Line-shape and polarization functions, the effective-mass approximation in the low-field limit. The fourth-rank tensorial form of Eq. (A2c) allows the general expression for $\Delta R/R$, Eq. (A3a), to be factored conveniently into lineshape and symmetry parts for a set of equivalent critical points whenever the effective-mass approximation is applicable. Let the unit vectors parallel to the field and polarization, and defined with respect to the crystal axes, be $\hat{\mathcal{E}}$ and $\hat{n}$, where $\hat{\mathcal{E}}=\mathcal{E}\,\hat{\mathcal{E}}$. Let $\vec{K}_{c1}=K_cK_1$ be the vector defined with respect to the crystal axes, locating the prototype critical point in the BZ. The complete set of critical points is generated by applying the set of symmetry operations of the crystal to $\vec{K}_{c1}$. Let $\hat{K}_\nu$ be the $\nu$th unit vector corresponding to the $\nu$th equivalent critical point in in this set.

We now break up the integral over the Brillouin zone in Eq. (A2c) into a summation of integrals, each a local integral about one of the equivalent critical points. In terms of local coordinates appropriate to the critical point $\nu$,

$$E_{cv}(\vec{k}-\vec{K}_{cv}) \cong E_g+\frac{\hbar^2k_T^2}{2\mu_T}+\frac{\hbar^2k_L^2}{2\mu_L} \quad , \tag{A4}$$

where $k_T$ and $k_L$ are the components of $\vec{k}-\vec{K}_{cv}$ perpendicular and parallel to $\hat{K}_\nu$, respectively. We assume local rotational symmetry around $\hat{K}_\nu$ for simplicity, whence the interband reduced-mass tensor has only two $k$-independent components in the effective-mass approximation. Using Eq. (A4), the contributions of the $\nu$th critical point to Eq. (A2a) can be written

$$\Delta\epsilon^\nu_{ij}(\hbar\omega,\vec{\mathcal{E}})=\left[\frac{e^4\hbar^4\mathcal{E}^2}{4\pi^2m^2E_+^2}\int_{1\mathrm{oc}}d^3k \times\left(E_g+\frac{\hbar^2k_T^2}{2\mu_T}+\frac{\hbar^2k_L^2}{2\mu_L}-E_+\right)^{-4}\right] \times P^{i,\nu}_{vc}\,P^{j,\nu}_{cv}\left(\frac{1-(\hat{\mathcal{E}}\cdot\hat{K}_\nu)^2}{\mu_T}+\frac{(\hat{\mathcal{E}}\cdot\hat{K}_\nu)^2}{\mu_L}\right) \quad , \tag{A5}$$

where the matrix elements $\vec{P}^\nu_{cv}$ depend only on $\vec{k}$ through the local optical selection rules (direction of $\vec{k}_\nu$). In the most important high-symmetry cases, the selection rule can usually be expressed as transverse allowed, parallel forbidden, where

$$n_in_jp^{i,\nu}_{vc}p^{j,\nu}_{cv}=1-(\hat{k}_\nu\cdot\hat{n})^2 \quad . \tag{A6}$$

Combining the above results we write finally

$$\frac{\Delta R}{R}=\left\{\left[\mathrm{Re}\;\tilde{C}\;\frac{e^4\hbar^4\mathcal{E}^2}{4\pi^2m^2E_+^2}\int_{1\mathrm{oc}}d^3k \times\left(E_g+\frac{\hbar^2k_T^2}{2\mu_T}+\frac{\hbar^2k_L^2}{2\mu_L}-\hbar\omega-i\Gamma\right)^{-4}\right]\right\} \times\left[\sum_\nu[1-(\hat{n}\cdot\hat{K}_\nu)^2]\left(\frac{1-(\hat{\mathcal{E}}\cdot\hat{K}_\nu)^2}{\mu_T}+\frac{(\hat{\mathcal{E}}\cdot\hat{K}_\nu)^2}{\mu_L}\right)\right] , \tag{A7}$$

where the first factor determines the line shape and the second factor is geometric and determines the polarization anisotropy. A phenomenological discussion of polarization effects, applicable specifically to the surface-barrier ER geometry and based entirely on the symmetry properties of these tensors, is given briefly in Sec. IID.

The line shapes predicted by Eq. (A7) can be evaluated by means of the following considerations. If $\mu_L$ is comparable to $\mu_T$, the integral can be extended to infinity in all three dimensions, and we obtain the three-dimensional low-field line shape

$$\left(\int_{1\text{oc}} d^3k \cdots\right)_{3D} = \frac{\pi^2}{8}\left(\frac{2\mu_T}{\hbar^2}\right)\left(\frac{2|\mu_L|}{\hbar^2}\right)^{1/2} \times \frac{i^{l+1}}{(\hbar\omega - E_g + i\Gamma)^{5/2}}\ , \quad \text{(A8)}$$

where $l$ is the critical-point order ($l=0$ if $\mu_L > 0$, $l=1$ if $\mu_L < 0$). If $\mu_L$ is extremely large, it is usually a better approximation to cut off the integral in the longitudinal direction and delete the term involving $\mu_L$ in the energy denominator. If $K_L$ is the effective length of the contributing region along the symmetry axis, we obtain in this case the two-dimensional line shape

$$\left(\int_{1\text{oc}} d^3k \cdots\right)_{2D} = \frac{\pi}{3}\left(\frac{2\mu_T}{\hbar^2}\right)\frac{-K_L}{(\hbar\omega - E_g + i\Gamma)^3}\ . \quad \text{(A9)}$$

These results will be used to extract critical point parameters from higher-energy critical-point structure in ER spectra.


[1]B. O. Seraphin, in *Proceedings of the Seventh International Conference on the Physics of Semiconductors*, edited by M. Hulin (Dunod, Paris, 1964), p. 165.

[2]M. Cardona, *Modulation Spectroscopy* (Academic, New York, 1969).

[3]See articles by B. O. Seraphin, R. L. Aggarwal, D. F. Blossey, and P. Handler, B. Batz, I. Balslev, and D. E. Aspnes, and N. Bottka, in *Semiconductors and Semimetals*, edited by R. K. Willardson and A. C. Beer (Academic, New York, 1972), Vol. 9.

[4]D. E. Aspnes and J. E. Rowe, Solid State Commun. **8**, 1145 (1970).

[5]D. E. Aspnes and J. E. Rowe, Phys. Rev. B **5**, 4022 (1972).

[6]D. E. Aspnes and J. E. Rowe, in *Proceedings of the Tenth International Conference on the Physics of Semiconductors*, edited by S. P. Keller, J. C. Hensel, and F. Stern (U.S. AEC Oak Ridge, Tenn., 1970), p. 422.

[7]D. E. Aspnes, Phys. Rev. Lett. **28**, 168 (1972).

[8]D. E. Aspnes, Phys. Rev. Lett. **28**, 913 (1972).

[9]D. E. Aspnes and A. Frova, Solid State Commun. **7**, 155 (1969).

[10]S. Koeppen and P. Handler, Phys. Rev. **187**, 1182 (1969).

[11]S. M. Sze, *Physics of Semiconductor Devices* (Wiley, New York, 1969).

[12]M. Chester and P. H. Wendtland, Phys. Rev. Lett. **13**, 193 (1964).

[13]V. A. Tyagai, V. B. Popov and O. V. Snitko, Fiz. Tekh. Poluprovodn. **6**, 179 (1972) [Sov. Phys.-Semicond. **6**, 148 (1972)].

[14]M. D. Sturge, Phys. Rev. **127**, 768 (1962).

[15]D. L. Greenaway, Phys. Rev. Lett. **9**, 97 (1962).

[16]B. O. Seraphin, J. Appl. Phys. **37**, 721 (1966); Proc. Phys. Soc. Lond. **87**, 239 (1966).

[17]M. Cardona, K. L. Shaklee, and F. H. Pollak, Phys. Rev. **154**, 696 (1967).

[18]V. Rehn and D. S. Kyser, Phys. Rev. Lett. **18**, 848 (1967).

[19]L. W. James, R. C. Eden, J. L. Moll, and W. E. Spicer, Phys. Rev. **174**, 909 (1968).

[20]W. E. Spicer and R. C. Eden in *Proceedings of the Ninth International Conference on the Physics of Semiconductors* (Nauka, Leningrad, 1968), p. 65.

[21]B. T. French, Phys. Rev. **174**, 991 (1968).

[22]E. Matatagui, A. G. Thompson, and M. Cardona, Phys. Rev. **176**,, 950 (1968).

[23]T. Nishino, M. Okuyama, and Y. Hamakawa, J. Phys. Chem. Solids **30**, 2671 (1969).

[24]R. A. Forman, D. E. Aspnes, and M. Cardona, J. Phys. Chem. Solids **31**, 227 (1970).

[25]D. S. Kyser and V. Rehn, Solid State Commun. **8**, 1437 (1970).

[26]R. R. Zucca and Y. R. Shen, Phys. Rev. B **1**, 2668 (1970).

[27]R. R. L. Zucca, J. P. Walter, Y. R. Shen, and M. L. Cohen, Solid State Commun. **8**, 627 (1970).

[28]D. D. Sell and S. E. Stokowski, in Ref. 6, p. 417.

[29]R. Braunstein and M. Welkowsky, in Ref. 6, p. 439.

[30]D. D. Sell, R. Dingle, S. E. Stokowski, and J. V. DiLorenzo, Phys. Rev. Lett. **27**, 1644 (1971).

[31]Yu. N. Berozashvili, A. V. Dundua, and D. Sh. Lordkipanidze, Fiz. Tverd. Tela **13**, 3172 (1971) [Sov. Phys.-Solid State **13**, 2669 (1972)].

[32]M. Welkowsky and R. Braunstein, Phys. Rev. B **5**, 497 (1972).

[33]V. Rehn and D. S. Kyser, Phys. Rev. Lett. **28**, 494 (1972).

[34]J. E. Rowe and S. Christman, Bull. Am. Phys. Soc. **17**, 367 (1972), and (unpublished).

[35]R. W. Koss and L. M. Lambert, Phys. Rev. B **5**, 1479 (1972).

[36]D. D. Sell, S. E. Stokowski, R. Dingle, and J. V. DiLorenzo, Phys. Rev. B **7**, 4568 (1973).

[37]D. D. Sell, in *Proceedings of the Eleventh International Conference on the Physics of Semiconductors* (PWN-Polish Scientific Publishers, Warsaw, 1972), p. 800.

[38]S. Pond and P. Handler, Phys. Rev. B (to be published).

[39]S. M. Sze, in Ref. 11, Chap. 8. See particularly Fig. 2 and Table 8.4 in this reference.

[40]J. D. E. McIntyre, Symp. Faraday Soc. **4**, 61 (1970).

[41]Number 217 Rhodium Plating Solution, manufactured by Engelhard Ind., 429 Delancy St., Newark, N. J. 07105.

[42]W. E. Dahlke and S. M. Sze, Solid-State Electron. **10**, 865 (1967).

[43]Manufactured by Monsanto Corp., St. Louis, Mo.

[44]B. R. Pruniaux and A. C. Adams, J. Appl. Phys. **43**, 1980 (1972).

[45]G. W. Eimers and E. H. Stevens, Solid-State Electron. **15**, 721 (1972).

[46]J. E. Fischer, Rev. Sci. Instrum. **42**, 872 (1971).

[47]M. Cardona, in Ref. 2. See Sec. 11 and 25.

[48]Type SC12 silver conducting paint, manufactured by Micro-Circuits Company, New Buffalo, Mich. It is essential that the conducting paint be well mixed before use. We found a magnetic stirrer to be ideal for this purpose.

[49]Copies of the data processing program are available upon request.

[50]S. M. Sze, in Ref. 11, pp. 368–393.

[51]K. Hesse and H. Strack, Solid-State Electron. **15**, 767 (1972).

[52]D. E. Aspnes, J. Electrochem. Soc. **116**, 585 (1969).

[53]D. E. Aspnes and J. E. Rowe, Bull. Am. Phys. Soc. **16**, 396 (1971), and (unpublished).

[54]D. E. Aspnes and J. E. Rowe, Phys. Rev. Lett. **27**, 188 (1971).

[55]E. Mohler, Phys. Status Solidi **29**, K55 (1968); Phys. Status Solidi **38**, 81 (1970).

[56]J. F. Nye, *Physical Properties of Crystals* (Oxford U. P., Oxford, England, 1957).

[57]E. O. Kane, Phys. Rev. **178**, 1368 (1969).

[58]D. D. Sell and E. O. Kane, Phys. Rev. **185**, 1103 (1969).

[59]N. Bottka and J. E. Fischer, Phys. Rev. B **3**, 2514 (1971).

[60]B. O. Seraphin, in *Optical Properties of Solids*, edited by E. Haidemenakis (Gordon and Breach, New York, 1970), p. 213.

[61]J. D. Zook, Phys. Rev. Lett. **20**, 848 (1968).

[62]V. A. Tyagai, V. N. Bondarenko, and O. V. Snitko, Fiz. Tekh. Poluprovodn. **5**, 1038 (1971) [Sov. Phys.-Semicond. 5, 920 (1971)]; F. Evangelisti, A. Frova, and J. U. Fischbach, Phys. Rev. Lett. **29**, 1001 (1972).
[63]L. V. Keldysh, O. V. Konstantinov, and V. I. Perel', Fiz. Tekh. Poluprovodn. **3**, 1042 (1969) [Sov. Phys.-Semicond. **3**, 876 (1970)].
[64]P. Lawaetz, Phys. Rev. B **4**, 3460 (1971).
[65]D. F. Blossey, Phys. Rev. B **2**, 3976 (1970); Phys. Rev. B **3**, 1382 (1971).
[66]J. D. Dow and D. Redfield, Phys. Rev. B **1**, 3358 (1970).
[67]F. C. Weinstein, J. D. Dow, and B. Y. Lao, Phys. Rev. B **4**, 3502 (1971).
[68]A more accurate line-shape analysis of the WDR measurements of Ref. 28 has been performed [D. D. Sell (private communication)], and yields an energy of $1855 \pm 2$ meV for the $n = 1$ exciton at the $E_0 + \Delta_0$ transition in GaAs at 2 °K. This value should replace the energy, $1850 \pm 5$ meV, reported in Ref. 28.
[69]F. H. Pollack, C. W. Higginbotham, and M. Cardona, J. Phys. Soc. Jap. Suppl. **21**, 20 (1966).
[70]M. L. Cohen and T. K. Bergstresser, Phys. Rev. **141**, 789 (1966).
[71]F. Herman, R. L. Kortum, C. D. Kuglin, J. P. Van Dyke, and S. Skillman, in *Methods of Computational Physics*, edited by B. Alder, S. Fernbach, and M. Rotenberg (Academic, New York, 1968), p. 193. See Table V.
[72]I. B. Ortenberger and W. E. Rudge (unpublished).
[73]M. Cardona and D. L. Greenaway, Phys. Rev. **125**, 1291 (1962).
[74]B. O. Seraphin and N. Bottka, Phys. Rev. **145**, 628 (1966).
[75]D. E. Aspnes (unpublished).
[76]J. E. Fischer, in Ref. 6, p. 427.
[77]D. E. Aspnes, Phys. Rev. **153**, 972 (1967). See also the listing of the functional forms in Tables II and III in D. E. Aspnes and N. Bottka, Ref. 3, p. 457.
[78]J. Grover, S. Koeppen, and P. Handler, Phys. Rev. B **4**, 2830 (1971).
[79]See Fig. 12 of Ref. 67.
[80]E. O. Kane, J. Phys. Chem. Solids **1**, 249 (1956).
[81]D. E. Aspnes, Phys. Rev. **147**, 554 (1966).
[82]J. E. Fischer and N. Bottka, Phys. Rev. Lett. **24**, 1292 (1970).
[83]E. Schmidt, Phys. Status Solidi B **45**, K39 (1971).
[84]G. G. Wepfer, T. C. Collins, and R. N. Euwema, Phys. Rev. B **4**, 1296 (1971).
[85]D. E. Aspnes and A. A. Studna, Solid State Commun. **11**, 1375 (1972).
[86]D. E. Aspnes, K. E. Benson, and A. A. Studna (unpublished).
[87]D. E. Aspnes, P. Handler, and D. F. Blossey, Phys. Rev. **166**, 921 (1968).
[88]J. E. Rowe and D. E. Aspnes, Phys. Rev. Lett. **25**, 162 (1970).

PHYSICAL REVIEW B VOLUME 7, NUMBER 10 15 MAY 1973

# Lattice Thermal Conductivity of Mercury Selenide*

Charles R. Whitsett, Donald A. Nelson, J. G. Broerman, and E. C. Paxhia†
*McDonnell Douglas Research Laboratories, McDonnell Douglas Corporation, St. Louis, Missouri 63166*
(Received 8 September 1972)

The lattice thermal conductivity between 1.7 and 270 K is reported for single crystals of mercury selenide having conduction electron concentrations from $2.1\times10^{17}$ to $6.7\times10^{18}$ cm$^{-3}$. The most striking feature of the data for HgSe is the pronounced depression of the magnitude of the thermal conductivity between 4 and 30 K, and this is attributed to the Wagner mechanism for third-order phonon-annihilation resonance scattering of phonons. The data were analyzed by using the Callaway formalism to determine the relaxation times for phonon scattering by normal and umklapp processes, point defects, resonance modes, crystal boundaries, and conduction electrons. The resonance dip in thermal conductivity was observed in variously prepared HgSe samples, including specially purified and vapor-deposited crystals. Addition of sulfur impurity to HgSe apparently enhanced the resonance scattering, but because sulfur considerably altered the normal and umklapp scattering it could not be concluded if substitutional sulfur atoms were the resonantly scattering centers or if they only indirectly affected the resonance. The ionized defects in HgSe, in concentrations corresponding to as many as $3\times10^{18}$ conduction electrons/cm$^3$, acted as point Rayleigh scattering centers, but there was no increase in the Rayleigh scattering as the electron concentration was increased above $3\times10^{18}$ cm$^{-3}$.

## I. INTRODUCTION

Mercury selenide (HgSe) is a II-VI compound with the same cubic zinc-blende structure as the well-known III-V semiconducting compounds.[1] However, like $\alpha$-Sn[2] and HgTe,[3] it is a zero-gap semiconductor or perfect semimetal by virtue of a symmetry-induced degeneracy of the valence-band maximum and conduction-band minimum.[4-6] Because of this peculiar band structure, the zero-gap semiconductors display a number of anomalous features in their dielectric,[7-9] transport,[10,11] and lattice dynamic behavior.[12] To understand the phonon interactions and defect properties of these structures, we have investigated the thermal-transport properties of HgSe.

We report here the thermal conductivity between 1.7 and 270 K of HgSe single crystals prepared in different ways and subjected to various annealing procedures. The low-temperature thermal con-